



University of Kentucky
UKnowledge

Theses and Dissertations--Electrical and
Computer Engineering

Electrical and Computer Engineering


2017

SPARSE DIRECT SOLUTION METHODS FOR CAPACITIVE EXTRACTION PROBLEMS ON CLOSELY-SPACED GEOMETRIES WITH HIGH ASPECT RATIOS

Chee Kean Chang

University of Kentucky, gckchang@hotmail.com

Author ORCID Identifier:

 <https://orcid.org/0000-0002-6156-8260>

Digital Object Identifier: <https://doi.org/10.13023/ETD.2017.371>

[Right click to open a feedback form in a new tab to let us know how this document benefits you.](#)

Recommended Citation

Chang, Chee Kean, "SPARSE DIRECT SOLUTION METHODS FOR CAPACITIVE EXTRACTION PROBLEMS ON CLOSELY-SPACED GEOMETRIES WITH HIGH ASPECT RATIOS" (2017). *Theses and Dissertations--Electrical and Computer Engineering*. 108.

https://uknowledge.uky.edu/ece_etds/108

This Master's Thesis is brought to you for free and open access by the Electrical and Computer Engineering at UKnowledge. It has been accepted for inclusion in Theses and Dissertations--Electrical and Computer Engineering by an authorized administrator of UKnowledge. For more information, please contact UKnowledge@lsv.uky.edu.

STUDENT AGREEMENT:

I represent that my thesis or dissertation and abstract are my original work. Proper attribution has been given to all outside sources. I understand that I am solely responsible for obtaining any needed copyright permissions. I have obtained needed written permission statement(s) from the owner(s) of each third-party copyrighted matter to be included in my work, allowing electronic distribution (if such use is not permitted by the fair use doctrine) which will be submitted to UKnowledge as Additional File.

I hereby grant to The University of Kentucky and its agents the irrevocable, non-exclusive, and royalty-free license to archive and make accessible my work in whole or in part in all forms of media, now or hereafter known. I agree that the document mentioned above may be made available immediately for worldwide access unless an embargo applies.

I retain all other ownership rights to the copyright of my work. I also retain the right to use in future works (such as articles or books) all or part of my work. I understand that I am free to register the copyright to my work.

REVIEW, APPROVAL AND ACCEPTANCE

The document mentioned above has been reviewed and accepted by the student's advisor, on behalf of the advisory committee, and by the Director of Graduate Studies (DGS), on behalf of the program; we verify that this is the final, approved version of the student's thesis including all changes required by the advisory committee. The undersigned agree to abide by the statements above.

Chee Kean Chang, Student

Dr. Robert J. Adams, Major Professor

Dr. Caicheng Lu, Director of Graduate Studies

SPARSE DIRECT SOLUTION METHODS FOR CAPACITIVE EXTRACTION
PROBLEMS ON CLOSELY-SPACED GEOMETRIES WITH HIGH ASPECT RATIOS

THESIS

A thesis submitted in partial fulfillment of the
requirements for the degree of Master of Science in
Electrical Engineering in the College of
Engineering at the University of Kentucky

By

Chee Kean Chang

San Jose, California

Director: Dr. Robert J. Adams

Lexington, Kentucky

2017

Copyright © Chee Kean Chang 2017

ABSTRACT OF THESIS

SPARSE DIRECT SOLUTION METHODS FOR CAPACITIVE EXTRACTION PROBLEMS ON CLOSELY-SPACED GEOMETRIES WITH HIGH ASPECT RATIOS

The method of moment (MoM) [1] is a widely used method in electromagnetics to solve static and dynamic electromagnetic problems on varying geometries. However, in closely spaced geometries coupled with large aspect ratios, e.g. a large parallel plate capacitor with very small separation gap, the problem exhibits several challenges. Firstly, the close proximity of the field and source elements presents problems with convergence in numerical evaluations of the interactions between them. Secondly, the aspect ratio of the geometry gives an approximation whereby to far field points, the source contributions from locations that are far apart appear to cancel each other. This leads to high condition numbers in the system matrix. This thesis explores the potential solution to these problems as well as the application of modular fast and direct (MFD) [2] solver to expedite the solution of such problems.

KEYWORDS: S-EFIE, GC Solver, Capacitance Extraction, MFD, AEFIEH-S,
Preconditioning

Chee Kean Chang

July 6, 2017

SPARSE DIRECT SOLUTION METHODS FOR CAPACITIVE EXTRACTION
PROBLEMS ON CLOSELY-SPACED GEOMETRIES WITH HIGH ASPECT RATIOS

By

Chee Kean Chang

Dr. Robert J. Adams

Director of Thesis

Dr. Caicheng Lu

Director of Graduate Studies

July 6, 2017

ACKNOWLEDGEMENTS

I wish to use this opportunity to convey my sincerest gratitude to all who supported this effort. First and foremost, to my parents who have been most encouraging and supportive of my decision to take a break from my career to complete my graduate studies despite their judgment and concern. They were most concerned with my adjustment from the industry back into the academia, as well as the financial stresses that my decision may incur.

I would also not have been able to progress towards completing my studies if not for Dr. Robert J. Adams' graciously taking me under his wing as his mentee and offering this problem as a topic of research for me to embark upon. This is despite all the annoyances of having to manage the fact that I am completing this remotely, thus precluding quick and easy access as any local student would have been able to afford him. Along the same vine, I want to thank Dr. Caicheng Lu for guiding me through all official channels in handling my extraordinary student status at The College of Engineering. I must also mention that I have inherited code from Dr. Lu that has tremendously contributed to the results of this research.

Thanks also to Dr. John C. Young who served in the thesis committee and shared his vast knowledge and experience in numerical integration methods. I wish to acknowledge his infectious enthusiasm in sharing his novel understanding in subjects that may otherwise be quite opaque to a new graduate student. This is most evident in his prompt responses to my queries and readiness to provide written explanations despite my queries coming in in the weekends! Many thanks to Dr. William T. Smith for graciously serving in my thesis committee, as well as starting my interest in focusing my studies in electromagnetics. Dr. Smith taught me EE522 in spring 2004.

Dr. Stephen Gedney, who is now associated with The University of Colorado at Denver, has also advised and encouraged me to complete my graduate studies by sharing with me options to fulfill my curriculum away from Lexington. I must also remark that, like Dr. Lu, Dr. Gedney has shared his code that contributed to the completion of this written work. Thank you for being a friend and kind teacher to me while I was in Lexington.

I will be most remiss if I do not also give thanks to the good Lord. Thank You for Your grace and inspiration.

TABLE OF CONTENTS

ACKNOWLEDGEMENTS	iii
TABLE OF CONTENTS	iv
LIST OF TABLES	vi
LIST OF FIGURES	vii
1 INTRODUCTION	1
2 THEORY	2
2.1 AEFIEnH-S Formulation	2
2.1.1 EFIE	2
2.1.2 Charge Continuity	7
2.1.3 $\mathbf{n} \cdot \mathbf{H}$ Constraint	7
2.1.4 Static Extraction	8
2.1.5 Application of Method of Moment	9
2.2 S-EFIE Formulation	13
2.3 GC Solver Formulation	16
2.4 Numerical Evaluation Methods	18
2.4.1 Potential Integrals	19
2.4.2 Extended Duffy Transform	23
2.5 Effects of Far Interactions	30
2.6 MFD and LOGOS	35
3 NUMERICAL RESULTS	42
3.1 Effects of Combined S-EFIE and GC Solver Formulation on Conditioning	42
3.2 Accuracy across Formulations	43
3.3 S-EFIE+GC Accuracy in Relation to Separation Delta	44
3.4 S-EFIE+GC Conditioning in Relation to Separation Delta	45
3.5 S-EFIE+GC Integrated with MFD Accuracy and Scalability Data	46
3.6 AEFIEnH-S with MFD Solution Accuracy	48

4 CONCLUSION	50
REFERENCES	51
VITA	53

LIST OF TABLES

Table 1:Definitions of parameters in the local coordinate system defined for each source triangle edge and the field point.....	20
Table 2:Condition numbers of S-EFIE and GC solver for 10m-by-10m parallel plate capacitor with 0.002m separation delta and 2028 DOFs.	35
Table 3:Result comparison of Q3D Extractor with S-EFIE, GC solver and S-EFIE+GC. Geometry is a 10m-by-10m parallel square plate capacitor with 0.002m separation delta.	44

LIST OF FIGURES

Figure 1:Regions V_1 and V_2 have the same constitutive parameters. Surface S is an imaginary surface binding sources J_2	2
Figure 2:Surface S_+ encloses volume V_2 and surface S is the surface of the PEC.	6
Figure 3: r_1^+ and r_1^- are the free vertices of $f_1(r)$ and T_1^+ and T_1^- are the positive and negative triangle cells of $f_1(r)$. The same naming convention is used for $f_2(r)$ and $f_3(r)$	14
Figure 4:Local coordinate system of edge 1 in relation to the field point projection onto the source triangle plane, which normal is in the z direction.....	21
Figure 5:Local coordinate system of edge 2 in relation to the field point projection onto the source triangle plane, which normal is in the z direction.....	22
Figure 6:Local coordinate system of edge 3 in relation to the field point projection onto the source triangle plane, which normal is in the z direction.....	23
Figure 7:Left is source triangle (LMN) in 3-dimensional global coordinate system and the right is source triangle (lmn) in 2-dimensional local coordinate system. O denotes the field point in global coordinates, o denotes the field point in local coordinates.	25
Figure 8: olm in local coordinate plane (left) maps to $o'l'm'o'$ in the Duffy plane (right)..	27
Figure 9:Field point (O) and source triangle (LMN) in global coordinates (left). Field point (o) and source triangle (lmn) in local coordinates (right).	29
Figure 10:Sub-trilaterals when field point is not in source triangle.....	30
Figure 11:Parallel plate capacitor with dimensions 10m-by-10m with 0.002m plate separation. There are 2028 triangles in the mesh; 1012 triangles on the top and bottom and 4 on the feed between the plates. The bottom and top plates have matching cell arrangements.	31
Figure 12:Effects of high aspect ratio and low separation delta between parallel capacitor plates on S-EFIE formulation.	32
Figure 13:Effects of high aspect ratio and low separation delta between parallel capacitor plates on GC solver formulation.	32
Figure 14:Joint effect of source triangles that are mutual images across the separation delta on a far field triangle.	33
Figure 15:Result of preconditioned S-EFIE system matrix compared to cases of lower aspect ratio.	34
Figure 16:Result of preconditioned GC solver system matrix compared to cases of lower aspect ratio.	34
Figure 17:A strip fitted with 3-level grid in MFD LOGOS factorization.....	36

Figure 18:The system matrix rearranged to match the LOGOS grid grouping. Localizing basis functions multiplied with system matrix yield excitation that is localized, non-localizing basis functions when multiplied result in excitation that reach the entire domain.	36
Figure 19:Level-3 factorization matrix structures.	37
Figure 20:Level-2 factorization matrix structures.	38
Figure 21:Steps to build the localizing and non-localizing basis function matrices.....	40
Figure 22:Condition number comparison for S-EFIE, GC solver and combined S-EFIE and GC solver formulations.	43
Figure 23:S-EFIE+GC formulation error relative to Q3D across 3 separation deltas for the same parallel square plate capacitor.....	45
Figure 24:S-EFIE+GC conditioning performance as separation delta decreases.	45
Figure 25:S-EFIE+GC with MFD formulation error relative to Q3D across 3 separation deltas for the same parallel square plate capacitor.....	46
Figure 26:DOF count versus fill operation scalability of S-EFIE+GC integrated with MFD compared to S-EFIE+GC dense fills.	47
Figure 27:MLSSM memory usage across different separation delta and DOF count.	47
Figure 28:DOF count versus LOGOS factorization CPU time.....	48
Figure 29:DOF count versus LOGOS solve CPU time.	48
Figure 30: AEFIE _n H-S dense run and with MFD run against analytical result for 1-m radius PEC sphere at 1.5m wavelength.....	49
Figure 31: AEFIE _n H-S dense run and with MFD run against analytical result for 1-m radius PEC sphere at 125m wavelength.....	49

1 INTRODUCTION

The method of moment (MoM) is a highly versatile method to solve static and dynamic electromagnetic problems due to its straightforward formulation. For example, in comparison with finite element method (FEM) [3], MoM does not require boundary truncation treatment like absorbing boundary condition [3] or perfectly matched layer [3] in open-boundary problems as the Green's function treats this. Also, in 3-dimensional problems, MoM can be formulated on surface discretization whereas FEM requires volumetric discretization. It is also worth mentioning that MoM affords more flexibility in the choice of basis functions since the formulation is based on integral equations instead of differential equations, which limits the pool of basis functions to those that are differentiable in the domain. However, the fact that it relies on accounting for the effect of a source to field point through convolution with a Green's function results in a matrix that is dense and therefore pose a problem on high memory usage to store the source to field interactions in the system matrix. A dense system matrix naturally implies that more computation time is spent on filling the matrix entries also. Thus, much research has been focused on mitigating these 2 problems.

On the aspect of increasing memory savings, solutions to compress the system matrix has been introduced. Use of modular fast direct (MFD) analysis method to resolve the issue is an alternative. However, MFD only works well with well-conditioned system matrices.

In this thesis, we focus on a 2 electrically isolated perfect electric conductor (PEC) capacitance computation problem where the geometry poses several challenges. Firstly, the conductors are very closely spaced and, secondly, the aspect ratio of the capacitor terminal largest edge to the terminal separation distance is high on the order of 5000 or more.

The challenges that are immediately at hand are the evaluation of system matrix entries where the source and field locations are mutually adjacent or separated by a minuscule gap, and the poor matrix conditioning. The second challenge is a roadblock to the use of MFD to achieve the goals of compute time and memory savings. Whereas, the first problem was found to be too cost prohibitive in computation time that even with MFD, the solution is not practically usable.

In this thesis, the first problem is handled with a of couple approaches; one extendable to allow quasi-static problem solution, and another which is strictly applicable to static problems only. In order to address the second problem, a preconditioning scheme is being attempted to address the poor conditioning of the system at high mesh density.

2 THEORY

2.1 AEFIE_nH-S Formulation

AEFIE_nH-S [4] is the augmented EFIE formulation [5]-[6] with a normal magnetic field constraint and a static charge subtraction from the formulation.

2.1.1 EFIE

This discussion shall begin with a simple derivation of the electric field integral equation approach using the equivalence surface current and extinction theories [7]. Given the following physical setup:

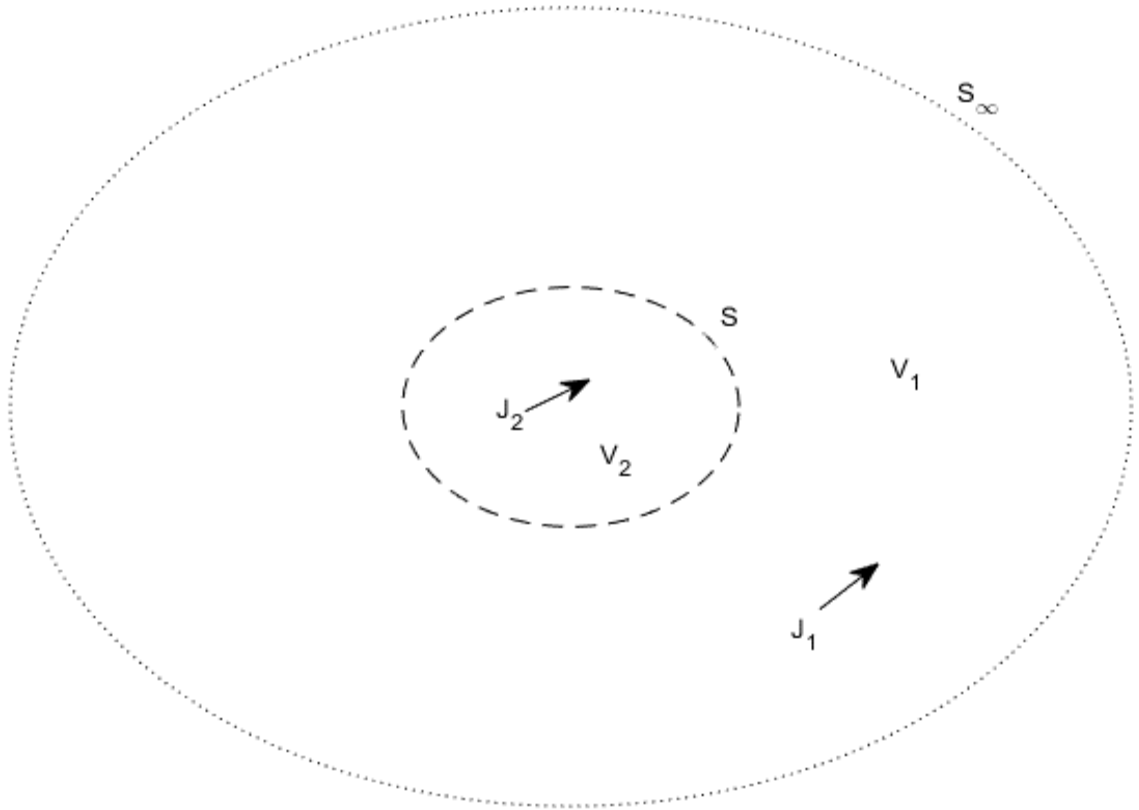


Figure 1:Regions V_1 and V_2 have the same constitutive parameters. Surface S is an imaginary surface binding sources J_2 .

Maxwell's equations [1] in the frequency domain with a time dependence of $e^{i\omega t}$ are as follows:

$$\nabla \times \vec{E}(\vec{r}) = -\vec{M}(\vec{r}) - i\omega\mu\vec{H}(\vec{r}) \quad (1)$$

$$\nabla \times \vec{H}(\vec{r}) = \vec{J}(\vec{r}) + i\omega\varepsilon\vec{E}(\vec{r}) \quad (2)$$

$$\nabla \cdot \vec{E}(\vec{r}) = \frac{\rho_e(\vec{r})}{\epsilon} \quad (3)$$

$$\nabla \cdot \vec{H}(\vec{r}) = \frac{\rho_m(\vec{r})}{\mu} \quad (4)$$

and charge continuity equation,

$$\nabla \cdot \vec{J}(\vec{r}) = -i\omega\rho_e(\vec{r}) \quad (5)$$

After the fact that magnetic current density and magnetic charge are not material, the terms $\vec{M}(\vec{r}) = 0$ and $\rho_m(\vec{r}) = 0$.

The Sommerfeld radiation condition [3] satisfied when electromagnetic waves propagate to great distances is as follows:

$$\lim_{|\vec{r}-\vec{r}'| \rightarrow \infty} |\vec{r}-\vec{r}'|(\nabla \times \vec{E}(\vec{r}) + ik\hat{r} \times \vec{E}(\vec{r})) = 0 \quad (6)$$

This essentially relates that at great distances from the source of propagation the electric and magnetic fields relations approximate those of plane waves.

The vector wave equation can be derived from Maxwell's equations as follows:

$$\begin{aligned} \nabla \times (\nabla \times \vec{E}(\vec{r})) &= \nabla \times (-\vec{M}(\vec{r}) - i\omega\mu\vec{H}(\vec{r})) \\ \nabla \times \nabla \times \vec{E}(\vec{r}) &= -i\omega\mu\nabla \times \vec{H}(\vec{r}) \\ \nabla \times \nabla \times \vec{E}(\vec{r}) &= -i\omega\mu(\vec{J}(\vec{r}) + i\omega\epsilon\vec{E}(\vec{r})) \\ \nabla \times \nabla \times \vec{E}(\vec{r}) - k^2\vec{E}(\vec{r}) &= -i\omega\mu\vec{J}(\vec{r}) \end{aligned} \quad (7)$$

The Green's function is a field response of a point source.

$$\vec{E}(\vec{r}) = -i\omega\mu \iiint \vec{J}(\vec{r}') \cdot \vec{G}(\vec{r}, \vec{r}') dV' \quad (8)$$

where

$$\vec{G}(\vec{r}, \vec{r}') = (\vec{I} + \frac{\nabla\nabla}{k^2}) \frac{e^{-ik|\vec{r}-\vec{r}'|}}{4\pi|\vec{r}-\vec{r}'|} \quad (9)$$

is the dyadic Green's function. It satisfies the Sommerfeld radiation condition and the expression is as follows [8]:

$$\lim_{|\vec{r}-\vec{r}'| \rightarrow \infty} |\vec{r}-\vec{r}'|(\nabla \times \vec{G}(\vec{r}, \vec{r}') + ik\hat{r} \times \vec{G}(\vec{r}, \vec{r}')) = 0 \quad (10)$$

Given this notion, the Green's function is expected to satisfy the vector wave equation as follows:

$$\begin{aligned}
& \nabla \times \nabla \times -i\omega\mu \iiint \vec{J}(\vec{r}') \cdot \vec{G}(\vec{r}, \vec{r}') dV' + k^2 i\omega\mu \iiint \vec{J}(\vec{r}') \cdot \vec{G}(\vec{r}, \vec{r}') dV' \\
& = -i\omega\mu \iiint \vec{J}(\vec{r}') \cdot \vec{I} \delta(\vec{r} - \vec{r}') dV' \\
& \nabla \times \nabla \times \vec{G}(\vec{r}, \vec{r}') - k^2 \vec{G}(\vec{r}, \vec{r}') = \vec{I} \delta(\vec{r} - \vec{r}') \tag{11}
\end{aligned}$$

If $\vec{G}(\vec{r}, \vec{r}')$ is multiplied into (7), and $\vec{E}(\vec{r})$ is multiplied into (11) and then (11) is subtracted from (7), the following expression results:

$$\nabla \times \nabla \times \vec{E}(\vec{r}) \cdot \vec{G}(\vec{r}, \vec{r}') - \nabla \times \nabla \times \vec{G}(\vec{r}, \vec{r}') \cdot \vec{E}(\vec{r}) = -i\omega\mu \vec{J}(\vec{r}) G(\vec{r}, \vec{r}') - \delta(\vec{r} - \vec{r}') \vec{E}(\vec{r}) \tag{12}$$

When (12) is integrated over volume V_1 , the following expression is arrived at

$$\begin{aligned}
& \iiint \nabla \times \nabla \times \vec{E}(\vec{r}) \cdot \vec{G}(\vec{r}, \vec{r}') - \nabla \times \nabla \times \vec{G}(\vec{r}, \vec{r}') \cdot \vec{E}(\vec{r}) dV_1 \\
& = \iiint -i\omega\mu \vec{J}(\vec{r}) G(\vec{r}, \vec{r}') - \delta(\vec{r} - \vec{r}') \vec{E}(\vec{r}) dV_1 \\
& \iiint \nabla \times \nabla \times \vec{E}(\vec{r}) \cdot \vec{G}(\vec{r}, \vec{r}') - \nabla \times \nabla \times \vec{G}(\vec{r}, \vec{r}') \cdot \vec{E}(\vec{r}) dV_1 = \vec{E}_1(\vec{r}') - \vec{E}(\vec{r}') \tag{13}
\end{aligned}$$

where

$$\vec{E}_1(\vec{r}') = \iiint -i\omega\mu \vec{J}(\vec{r}) G(\vec{r}, \vec{r}') dV_1 \tag{14}$$

and

$$\vec{E}(\vec{r}') = \iiint \delta(\vec{r} - \vec{r}') \vec{E}(\vec{r}) dV_1 \tag{15}$$

In the above expression, $\vec{E}(\vec{r}')$ is the total electric field in V_1 and $\vec{E}_1(\vec{r}')$ is the electric field in V_1 contributed by the source $\vec{J}_1(\vec{r})$ in V_1 . The left-hand side of (13) may be changed using the following identity:

$$\begin{aligned}
& \nabla \cdot [\vec{E}(\vec{r}) \times \nabla \times \vec{G}(\vec{r}, \vec{r}') + \nabla \times \vec{E}(\vec{r}) \times \vec{G}(\vec{r}, \vec{r}')] \\
& = \nabla \times \nabla \times \vec{E}(\vec{r}) \cdot \vec{G}(\vec{r}, \vec{r}') - \nabla \times \nabla \times \vec{G}(\vec{r}, \vec{r}') \cdot \vec{E}(\vec{r})
\end{aligned}$$

If the divergence theorem is then applied, the final left-hand side becomes the following:

$$\begin{aligned}
& - \iint [\vec{E}(\vec{r}) \times \nabla \times \vec{G}(\vec{r}, \vec{r}') + \nabla \times \vec{E}(\vec{r}) \times \vec{G}(\vec{r}, \vec{r}')] \cdot \hat{n} dS_\infty \\
& - \iint [\vec{E}(\vec{r}) \times \nabla \times \vec{G}(\vec{r}, \vec{r}') + \nabla \times \vec{E}(\vec{r}) \times \vec{G}(\vec{r}, \vec{r}')] \cdot \hat{n} dS
\end{aligned}$$

Note that the normal vector \hat{n} points into the region V_1 , hence the above surface integral expressions are negated. The kernel of the first term integral in the left-hand side cancels out after substitution of the Sommerfeld radiation conditions into it as follows:

$$\begin{aligned}
& - \iint [\vec{E}(\vec{r}) \times \nabla \times \bar{G}(\vec{r}, \vec{r}') + \nabla \times \vec{E}(\vec{r}) \times \bar{G}(\vec{r}, \vec{r}')] \cdot \hat{n} dS_\infty \\
& = - \iint [\vec{E}(\vec{r}) \times (-ik\vec{r} \times \bar{G}(\vec{r}, \vec{r}')) + (-ik\vec{r} \times \vec{E}(\vec{r})) \times \bar{G}(\vec{r}, \vec{r}')] \cdot \hat{n} dS_\infty \\
& = - \iint [ik\vec{r} \times \vec{E}(\vec{r}) \times \bar{G}(\vec{r}, \vec{r}') - ik\vec{r} \times \vec{E}(\vec{r}) \times \bar{G}(\vec{r}, \vec{r}')] \cdot \hat{n} dS_\infty \\
& = 0
\end{aligned}$$

Thus, (13) can now be written as follows:

$$- \iint [\vec{E}(\vec{r}) \times \nabla \times \bar{G}(\vec{r}, \vec{r}') + \nabla \times \vec{E}(\vec{r}) \times \bar{G}(\vec{r}, \vec{r}')] \cdot \hat{n} dS = \vec{E}_1(\vec{r}') - \vec{E}(\vec{r}')$$

With vector identity manipulations, this expression can be changed to the following:

$$\begin{aligned}
& \iint \hat{n} \cdot (\vec{E}(\vec{r}) \times (\nabla \times \bar{G}(\vec{r}, \vec{r}'))) + \hat{n} \cdot ((\nabla \times \vec{E}(\vec{r})) \times \bar{G}(\vec{r}, \vec{r}')) dS = -\vec{E}_1(\vec{r}') + \vec{E}(\vec{r}') \\
& \iint (\nabla \times \bar{G}(\vec{r}, \vec{r}')) \cdot (\hat{n} \times \vec{E}(\vec{r})) + \hat{n} \cdot (-i\omega\mu\vec{H}(\vec{r}) \times \bar{G}(\vec{r}, \vec{r}')) dS = -\vec{E}_1(\vec{r}') + \vec{E}(\vec{r}') \\
& \iint (\nabla \times \bar{G}(\vec{r}, \vec{r}')) \cdot (\hat{n} \times \vec{E}(\vec{r})) + \bar{G}(\vec{r}, \vec{r}') \cdot (\hat{n} \times -i\omega\mu\vec{H}(\vec{r})) dS = -\vec{E}_1(\vec{r}') + \vec{E}(\vec{r}')
\end{aligned}$$

It is recognized that $\hat{n} \times \vec{E}(\vec{r})$ is, by boundary condition, the surface magnetic current density $-\vec{M}_s(\vec{r})$, and $\hat{n} \times -\vec{H}(\vec{r})$ is the surface electric current density $-\vec{J}_s(\vec{r})$. Hence, the following expression is arrived at:

$$\begin{aligned}
& \iint (\nabla \times \bar{G}(\vec{r}, \vec{r}')) \cdot (-\vec{M}_s(\vec{r})) - i\omega\mu \bar{G}(\vec{r}, \vec{r}') \cdot \vec{J}_s(\vec{r}) dS = -\vec{E}_1(\vec{r}') + \vec{E}(\vec{r}') \\
& -i\omega\mu \iint \bar{G}(\vec{r}, \vec{r}') \cdot \vec{J}_s(\vec{r}) dS + \vec{E}_1(\vec{r}') = \vec{E}(\vec{r}')
\end{aligned}$$

It must be noted from the formulation thus far the vector \vec{r}' does not mean the coordinate vector of sources, but of an arbitrary field point in this case under study; i.e. any point in V_1 or V_2 . The vector \vec{r} whilst also representing an arbitrary location vector in the setup is limited to be within the V_1 region due to the volume limits of the integration. In the interest of minimizing confusion, the coordinate notations are exchanged. Therefore:

$$-i\omega\mu \iint \bar{G}(\vec{r}, \vec{r}') \cdot \vec{J}_s(\vec{r}') dS' + \vec{E}_1(\vec{r}) = \vec{E}(\vec{r}) \quad (16)$$

Here, $\vec{E}_1(\vec{r})$ is the electric field in V_1 resulting from the sources in V_1 , $\vec{J}_s(\vec{r}')$ is the equivalent surface current density on the bounding surface S , where \vec{r}' indicates position vectors on the surface S . This equivalent surface current on the boundary S satisfies the uniqueness of the field

generated by the sources in V_2 on the boundary and outside it whilst extinguishing fields in V_2 . $\vec{E}(\vec{r})$ is the total field observed in V_1 .

This concept can then be applied to a setup depicted in Figure 2.

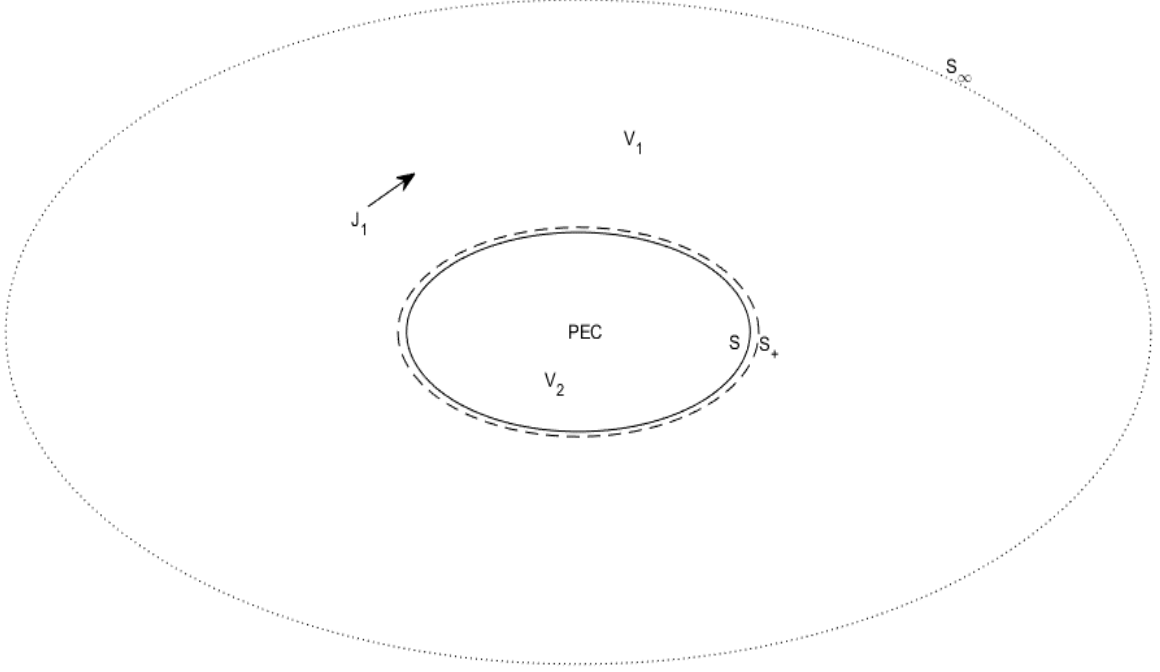


Figure 2: Surface S_+ encloses volume V_2 and surface S is the surface of the PEC.

In this case, $\vec{E}_1(\vec{r})$ is the electric field contributed by \vec{J}_1 and is the incident electric field, \vec{E}^{inc} . When \vec{E}^{inc} impinges on the perfect electric conductor (PEC), a surface electric current density, \vec{J}_S , is induced on S . The effect of \vec{J}_S in the V_1 region can be generated by an equivalence surface current on S_+ that is just large enough to bound surface S , which will be denoted \vec{J}_{Seq} , in place of \vec{J}_S . Expression (16) can be used in this context as follows:

$$-i\omega\mu \iint \bar{G}(\vec{r}, \vec{r}') \cdot \vec{J}_{Seq}(\vec{r}') dS'_+ + \vec{E}^{inc}(\vec{r}) = \vec{E}(\vec{r})$$

where $\vec{r} \in S$.

In this case, the integral term is the scattered electric field, \vec{E}^{scat} . The boundary condition on a PEC dictates that on S , $\vec{E}^t(\vec{r}) = 0$. Therefore, $\vec{E}^{scat t}(\vec{r}) = -\vec{E}^{inc t}(\vec{r})$. Such an arrangement allows the PEC to be removed without affecting the field in V_1 . After the fact that S_+ is very close to S , \vec{J}_{Seq} is effectively \vec{J}_S . This is the EFIE formulation. Therefore,

$$i\omega\mu \iint \bar{G}(\vec{r}, \vec{r}') \cdot \vec{J}_S(\vec{r}') dS' = \vec{E}^{inc t}(\vec{r}) \quad (17)$$

Note that this formulation is applicable to closed as well as open surfaces as long as no magnetic current density is present on the boundary; implying continuous tangential electric field across the boundary.

The dynamic EFIE formulation in expanded form from (17) is as follows:

$$i\omega\mu \iint G(\vec{r}, \vec{r}') \vec{J}_S(\vec{r}') dS' + \frac{i}{\omega\epsilon} \iint \nabla (\nabla' \cdot \vec{J}_S(\vec{r}') G(\vec{r}, \vec{r}')) dS' = \vec{E}^{inc}(\vec{r}) \quad (18)$$

However, to express (18) in terms of the whole electric field instead of just its component that is tangential to the incident surface, it can be written as:

$$i\omega\mu\hat{n} \times \iint G(\vec{r}, \vec{r}') \vec{J}_S(\vec{r}') dS' + \frac{i}{\omega\epsilon} \hat{n} \times \iint \nabla (\nabla' \cdot \vec{J}_S(\vec{r}') G(\vec{r}, \vec{r}')) dS' = \hat{n} \times \vec{E}^{inc}(\vec{r}) \quad (19)$$

where

$$G(\vec{r}, \vec{r}') = \frac{e^{-ik|\vec{r}-\vec{r}'|}}{4\pi|\vec{r}-\vec{r}'|} \quad (20)$$

The charge continuity equation can be substituted into (19) and give:

$$\begin{aligned} i\omega\mu\hat{n} \times \iint G(\vec{r}, \vec{r}') \vec{J}_S(\vec{r}') dS' + \frac{1}{\epsilon} \hat{n} \times \iint \nabla (\rho_e(\vec{r}') G(\vec{r}, \vec{r}')) dS' &= \hat{n} \times \vec{E}^{inc}(\vec{r}) \\ ik\hat{n} \times \iint G(\vec{r}, \vec{r}') \vec{J}_S(\vec{r}') dS' + c\hat{n} \times \iint \nabla (\rho_e(\vec{r}') G(\vec{r}, \vec{r}')) dS' &= \frac{1}{\eta} \hat{n} \times \vec{E}^{inc}(\vec{r}) \\ ik\hat{n} \times \iint G(\vec{r}, \vec{r}') \vec{J}_S(\vec{r}') dS' + c\hat{n} \times \iint \rho_e(\vec{r}') \nabla G(\vec{r}, \vec{r}') dS' &= \frac{1}{\eta} \hat{n} \times \vec{E}^{inc}(\vec{r}) \end{aligned} \quad (21)$$

2.1.2 Charge Continuity

In order to form the Augmented EFIE formulation, the charge continuity constraint (5) is also enforced in addition to (21). In the interest of improving the conditioning of the system matrix, constraint (5) is convolved with the Green's function $G(\vec{r}, \vec{r}')$. Thus giving,

$$\iint G(\vec{r}, \vec{r}') \nabla \cdot \vec{J}_S(\vec{r}') ds' + i\omega \iint G(\vec{r}, \vec{r}') \rho_e(\vec{r}') ds' = 0 \quad (22)$$

2.1.3 $\hat{n} \cdot \vec{H}$ Constraint

The $\hat{n} \cdot \vec{H}$ component of AEFIE_{NH-S} is derived from (21) by taking its divergence:

$$\begin{aligned} \nabla \cdot \left(ik\hat{n} \times \iint G(\vec{r}, \vec{r}') \vec{J}_S(\vec{r}') dS' \right) + \nabla \cdot \left(c\hat{n} \times \iint \nabla (\rho_e(\vec{r}') G(\vec{r}, \vec{r}')) dS' \right) \\ = \nabla \cdot \left(\frac{1}{\eta} \hat{n} \times \vec{E}^{inc}(\vec{r}) \right) \end{aligned}$$

$$\begin{aligned}
& -ik\hat{n} \cdot \left(\nabla \times \iint G(\vec{r}, \vec{r}') \vec{J}_S(\vec{r}') dS' \right) - c\hat{n} \cdot \left(\nabla \times \iint \nabla(\rho_e(\vec{r}') G(\vec{r}, \vec{r}')) dS' \right) \\
& = -\frac{1}{\eta} \hat{n} \cdot \left(\nabla \times \vec{E}^{inc}(\vec{r}) \right) \\
& -\hat{n} \cdot \left(\nabla \times \iint G(\vec{r}, \vec{r}') \vec{J}_S(\vec{r}') dS' \right) = \hat{n} \cdot \vec{H}^{inc}(\vec{r}) \\
& \iint \nabla G(\vec{r}, \vec{r}') \cdot (\hat{n} \times \vec{J}_S(\vec{r}')) dS' = \hat{n} \cdot \vec{H}^{inc}(\vec{r}) \tag{23}
\end{aligned}$$

Charge neutrality is also enforced on all electrically isolated surfaces.

2.1.4 Static Extraction

The -S component originated from a problem found where AEFIE_nH yields high condition numbers at low frequencies for multiply connected geometries. As seen thus far, the AEFIE formulation used does not place a ik multiplier on the current density as in [5]-[6], but remains with the vector potential term of (21). The $\hat{n} \cdot \vec{H}$ constraint is actually intended to counter the problem by constraining the current densities in the absence of the vector potential term of EFIE. However, it is also reported in [9] that the constraint has a null space on cases with multiply connected geometry. Therefore, uniqueness is not guaranteed and is manifested as high condition number. Close observation of the problem at frequencies approaching zero however indicates that the problem starts to resemble a static field problem. Therefore, to equalize the contribution from the charges on the scalar potential term with the current density on the vector potential term, the contribution from static charges are deducted from the system.

As such, the incident electric field and charge density in the system are decomposed into dynamic and static components. The static incident electric field is denoted $\vec{E}_0^{inc}(\vec{r})$ and is cancelled by a static scattered electric field $\vec{E}_0^{scat}(\vec{r})$ at the PEC boundary that is generated by a static surface charge density on the PEC denoted as $\rho_0(\vec{r}')$. Since this is a static field case, this phenomenon can be summarized by expression (21) with $k = 0$, $\rho_e(\vec{r}') = \rho_0(\vec{r}')$, and $\vec{E}^{inc}(\vec{r}) = \vec{E}_0^{inc}(\vec{r})$, thus giving:

$$c\hat{n} \times \iint \rho_0(\vec{r}') \nabla G_0(\vec{r}, \vec{r}') dS' = \frac{1}{\eta} \hat{n} \times \vec{E}_0^{inc}(\vec{r}) \tag{24}$$

where

$$G_0(\vec{r}, \vec{r}') = \frac{1}{4\pi|\vec{r} - \vec{r}'|} \tag{25}$$

The ultimate intention is to have an expression that accounts for the current density that yields the dynamic scattered electric field to cancel the dynamic incident electric field $\vec{E}_k^{inc}(\vec{r})$ at the PEC

boundary as the excitation frequency diminishes. To this end, the total incident electric $\vec{E}^{inc}(\vec{r})$ field is expressed as:

$$\vec{E}^{inc}(\vec{r}) = ik\vec{E}_k^{inc}(\vec{r}) + \vec{E}_0^{inc}(\vec{r}) \quad (26)$$

In such an arrangement, as the excitation frequency diminishes (i.e., $k \rightarrow 0$) $\vec{E}^{inc}(\vec{r}) \approx \vec{E}_0^{inc}(\vec{r})$. The object is to have (21) solve for excitation $\vec{E}^{inc}(\vec{r}) - \vec{E}_0^{inc}(\vec{r})$ on the right-hand side. Thus, (21) needs to have (24) deducted from it. Before this can be done, the charge density needs to be redefined as being constituted from static charge density, which yields the static scattered electric field to counter the static incident electric field on the PEC boundary, and dynamic charge density $\rho_k(\vec{r}')$, which represent the moving charges that give rise to the charge continuity constraint in dynamic cases. Thus,

$$\rho_e(\vec{r}') = ik\rho_k(\vec{r}') + \rho_0(\vec{r}') \quad (27)$$

Much like the excitation, as frequency diminishes (i.e., $k \rightarrow 0$) $\rho_e(\vec{r}') \approx \rho_0(\vec{r}')$. With these premises, (21) is rewritten as follows:

$$\begin{aligned} ik\hat{n} \times \iint G(\vec{r}, \vec{r}') \vec{J}_S(\vec{r}') dS' + c\hat{n} \times \iint (ik\rho_k(\vec{r}') + \rho_0(\vec{r}')) \nabla G(\vec{r}, \vec{r}') dS' \\ = \frac{1}{\eta} \hat{n} \times (ik\vec{E}_k^{inc}(\vec{r}) + \vec{E}_0^{inc}(\vec{r})) \\ \hat{n} \times \iint G(\vec{r}, \vec{r}') \vec{J}_S(\vec{r}') dS' + \hat{n} \times \iint (c\rho_k(\vec{r}')) \nabla G(\vec{r}, \vec{r}') dS' \\ = \frac{\hat{n}}{ik\eta} \times \vec{E}^{inc}(\vec{r}) - \frac{\hat{n}}{ik} \times \iint c\rho_0(\vec{r}') \nabla G(\vec{r}, \vec{r}') dS' \end{aligned} \quad (28)$$

Note that the new representation of $\rho_e(\vec{r}')$ affects the charge continuity constraint (22) as follows:

$$\begin{aligned} \iint G(\vec{r}, \vec{r}') \nabla \cdot \vec{J}_S(\vec{r}') ds' + i\omega \iint G(\vec{r}, \vec{r}') (ik\rho_k(\vec{r}') + \rho_0(\vec{r}')) ds' = 0 \\ \iint G(\vec{r}, \vec{r}') \nabla \cdot \vec{J}_S(\vec{r}') ds' + \frac{i\omega}{c} \iint G(\vec{r}, \vec{r}') (ikc\rho_k(\vec{r}') + c\rho_0(\vec{r}')) ds' = 0 \\ \iint G(\vec{r}, \vec{r}') \nabla \cdot \vec{J}_S(\vec{r}') ds' - k^2 \iint G(\vec{r}, \vec{r}') c\rho_k(\vec{r}') ds' = -ik \iint c\rho_0(\vec{r}') G(\vec{r}, \vec{r}') ds' \end{aligned} \quad (29)$$

Thus, expressions (23), (28), (29) along with the charge neutrality constraints for each electrically isolated surface conclude the necessary constraints to construct the AEFIE_nH-S system.

2.1.5 Application of Method of Moment

The method of moment is then used to solve for the current densities and dynamic charges. The subject geometry is first approximated with a mesh of N_t triangles with each triangle denoted as T_n where $n = 1, 2, \dots, N_t$. In this approximate geometry, N_e internal edges are

defined. An internal edge is defined as an edge that is shared by a pair of triangles. $\vec{J}_S(\vec{r})$ is approximated by a summation of RWG [10] basis functions. RWG functions are defined for internal edges that are shared by a couple of triangles. One of the triangles in the triangle pair is designated as the positive triangle, T_n^+ , and the other designated the negative triangle, T_n^- . There is 1 free vertex associated with each of the triangles in the pair and is the triangle vertex that is not shared with the other triangle in the pair; designated \vec{r}_n^+ and \vec{r}_n^- for the positive triangle free vertex and negative triangle free vertex respectively. The formal definition of a RWG function, $\vec{f}_n(\vec{r})$, is as follows:

$$\vec{f}_n(\vec{r}) = \begin{cases} \frac{e_n(\vec{r} - \vec{r}_n^+)}{2A_n^+}, & \vec{r} \in T_n^+ \\ \frac{e_n(\vec{r}_n^- - \vec{r})}{2A_n^-}, & \vec{r} \in T_n^- \\ 0, & \text{elsewhere} \end{cases} \quad (30)$$

$$\vec{J}_S(\vec{r}') \approx \sum_{n=1}^{N_e} j_n \vec{f}_n(\vec{r}') \quad (31)$$

where e_n is the length of internal edge $n = 1, 2, \dots, N_e$. $\rho_e(\vec{r}')$ shall be approximated with a summation of subdomain pulse basis functions, $h_n(\vec{r})$, defined as:

$$h_n(\vec{r}) = \begin{cases} \frac{1}{A_n}, & \vec{r} \in T_n \\ 0, & \vec{r} \notin T_n \end{cases} \quad (32)$$

$$\rho_e(\vec{r}') \approx \sum_{n=1}^{N_t} q_n h_n(\vec{r}') \quad (33)$$

q_n is therefore the total charge in T_n .

The constraints are then tested with a set of test functions to yield a set of linear algebraic equations. If $W(\vec{r})$ and $X(\vec{r})$ are scalar functions where $W(\vec{r})$ is the test or weighting function and $X(\vec{r})$ is the basis function, the testing procedure is defined as

$$\langle W(\vec{r}), X(\vec{r}) \rangle = \iint W(\vec{r}) X(\vec{r}) dS \quad (34)$$

If the test and basis functions are vector functions, the procedure is as follows:

$$\langle \vec{W}(\vec{r}), \vec{X}(\vec{r}) \rangle = \iint \vec{W}(\vec{r}) \cdot \vec{X}(\vec{r}) dS \quad (35)$$

The EFIE constraint is tested with N_e RWG functions, the charge continuity constraint is tested with N_t pulse basis functions, and the $\hat{n} \cdot \vec{H}$ constraint is tested with N_e divergence of the Buffa-Christiansen(BC) [11] functions which is denoted as $\vec{f}_m^b(\vec{r})$. The charge neutrality constraint is

not tested and is simply a function indicating that the sum of charges on an electrically isolated surface total to zero. Hence, the following expressions result:

$$\begin{aligned}
& \iint (\hat{n} \times \vec{f}_m(\vec{r})) \cdot \left(\hat{n} \times \iint G(\vec{r}, \vec{r}') \sum_{n=1}^{N_e} j_n \vec{f}_n(\vec{r}') dS' \right) dS \\
& + \iint (\hat{n} \times \vec{f}_m(\vec{r})) \cdot \left(\hat{n} \times \iint c \sum_{n=1}^{N_t} q_{kn} h_n(\vec{r}') \nabla G(\vec{r}, \vec{r}') dS' \right) dS \\
& = \frac{1}{ik\eta} \iint (\hat{n} \times \vec{f}_m(\vec{r})) \cdot (\hat{n} \times \vec{E}^{inc}(\vec{r})) dS \\
& - \frac{1}{ik} \iint (\hat{n} \times \vec{f}_m(\vec{r})) \cdot (\hat{n} \times \iint c \sum_{n=1}^{N_t} q_{0n} h_n(\vec{r}') \nabla G(\vec{r}, \vec{r}') dS') dS
\end{aligned}$$

$$\begin{aligned}
& \iint \vec{f}_m(\vec{r}) \cdot \iint G(\vec{r}, \vec{r}') \sum_{n=1}^{N_e} j_n \vec{f}_n(\vec{r}') dS' dS \\
& + \iint \vec{f}_m(\vec{r}) \cdot \iint c \sum_{n=1}^{N_t} q_{kn} h_n(\vec{r}') \nabla G(\vec{r}, \vec{r}') dS' dS \\
& = \frac{1}{ik\eta} \iint \vec{f}_m(\vec{r}) \cdot \vec{E}^{inc}(\vec{r}) dS \\
& - \frac{1}{ik} \iint \vec{f}_m(\vec{r}) \cdot \iint c \sum_{n=1}^{N_t} q_{0n} h_n(\vec{r}') \nabla G(\vec{r}, \vec{r}') dS' dS
\end{aligned}$$

$$\begin{aligned}
& \iint \vec{f}_m(\vec{r}) \cdot \iint G(\vec{r}, \vec{r}') \sum_{n=1}^{N_e} j_n \vec{f}_n(\vec{r}') dS' dS \\
& - \iint \nabla \cdot \vec{f}_m(\vec{r}) \iint c \sum_{n=1}^{N_t} q_{kn} h_n(\vec{r}') G(\vec{r}, \vec{r}') dS' dS \\
& = \frac{1}{ik\eta} \iint \vec{f}_m(\vec{r}) \cdot \vec{E}^{inc}(\vec{r}) dS \\
& + \frac{1}{ik} \iint \nabla \cdot \vec{f}_m(\vec{r}) \iint c \sum_{n=1}^{N_t} q_{0n} h_n(\vec{r}') G(\vec{r}, \vec{r}') dS' dS
\end{aligned}$$

$$\begin{aligned}
& \sum_{n=1}^{N_e} j_n \iint \vec{f}_m(\vec{r}) \cdot \iint G(\vec{r}, \vec{r}') \vec{f}_n(\vec{r}') dS' dS \\
& - \sum_{n=1}^{N_t} c q_{kn} \iint \nabla \cdot \vec{f}_m(\vec{r}) \iint h_n(\vec{r}') G(\vec{r}, \vec{r}') dS' dS \\
& = \frac{1}{ik\eta} \iint \vec{f}_m(\vec{r}) \cdot \vec{E}^{inc}(\vec{r}) dS
\end{aligned} \tag{36}$$

$$\begin{aligned}
& + \frac{1}{ik} \sum_{n=1}^{N_t} c q_{0n} \iint \nabla \cdot \vec{f}_m(\vec{r}) \iint h_n(\vec{r}') G(\vec{r}, \vec{r}') dS' dS \\
& \iint h_m(\vec{r}) \iint G(\vec{r}, \vec{r}') \nabla \cdot \sum_{n=1}^{N_e} j_n \vec{f}_n(\vec{r}') dS' dS \\
& - k^2 \iint h_m(\vec{r}) \iint G(\vec{r}, \vec{r}') c \sum_{n=1}^{N_t} q_{kn} h_n(\vec{r}') dS' dS \\
& = -ik \iint h_m(\vec{r}) \iint c \sum_{n=1}^{N_t} q_{0n} h_n(\vec{r}') G(\vec{r}, \vec{r}') dS' dS
\end{aligned}$$

$$\begin{aligned}
& \sum_{n=1}^{N_e} j_n \iint h_m(\vec{r}) \iint G(\vec{r}, \vec{r}') \nabla \cdot \vec{f}_n(\vec{r}') dS' dS \\
& - k^2 \sum_{n=1}^{N_t} c q_{kn} \iint h_m(\vec{r}) \iint G(\vec{r}, \vec{r}') h_n(\vec{r}') dS' dS \\
& = -ik \sum_{n=1}^{N_t} c q_{0n} \iint h_m(\vec{r}) \iint h_n(\vec{r}') G(\vec{r}, \vec{r}') dS' dS
\end{aligned} \tag{37}$$

$$\iint \nabla \cdot \vec{f}_m^b(\vec{r}) \iint \nabla G(\vec{r}, \vec{r}') \cdot \left(\hat{n} \times \sum_{n=1}^{N_e} j_n \vec{f}_n(\vec{r}') \right) dS' dS = \iint \nabla \cdot \vec{f}_m^b(\vec{r}) \hat{n} \cdot \vec{H}^{inc}(\vec{r}) dS$$

$$\sum_{n=1}^{N_e} j_n \iint \nabla \cdot \vec{f}_m^b(\vec{r}) \iint \nabla G(\vec{r}, \vec{r}') \cdot (\hat{n} \times \vec{f}_n(\vec{r}')) dS' dS = \iint \nabla \cdot \vec{f}_m^b(\vec{r}) \hat{n} \cdot \vec{H}^{inc}(\vec{r}) dS \tag{38}$$

These expressions form a system of equations that can be represented in matrix form as follows:

$$\begin{bmatrix} \mathbf{L}_A & \mathbf{L}_q \\ \mathbf{D}_J & -k^2 \mathbf{D}_q \\ \mathbf{Q} & \mathbf{0} \\ \mathbf{0} & \mathbf{N}_q \end{bmatrix} \begin{bmatrix} \mathbf{j} \\ [c\mathbf{q}_k] \end{bmatrix} = \frac{1}{ik} \left(\frac{1}{\eta} \begin{bmatrix} \mathbf{b}_{tE} \\ \mathbf{0} \\ ik\eta \mathbf{b}_{nH} \\ \mathbf{0} \end{bmatrix} - \begin{bmatrix} \mathbf{L}_q \\ -k^2 \mathbf{D}_q \\ \mathbf{0} \\ \mathbf{0} \end{bmatrix} [c\mathbf{q}_0] \right) \tag{39}$$

where \mathbf{L}_A and \mathbf{Q} are $N_e \times N_e$ matrices, \mathbf{L}_q is a $N_e \times N_t$ matrix, \mathbf{D}_J is a $N_t \times N_e$ matrix, \mathbf{D}_q is a $N_t \times N_t$ matrix, \mathbf{b}_{tE} and \mathbf{b}_{nH} are $N_e \times 1$ vectors, and \mathbf{q}_k and \mathbf{q}_0 are $N_t \times 1$ vectors. \mathbf{N}_q is a $N_o \times N_t$ matrix, where N_o is the number of electrically isolated surfaces in the geometry.

The definitions of the submatrices' elements are as follows:

$$[\mathbf{L}_A]_{mn} = \iint \vec{f}_m(\vec{r}) \cdot \iint G(\vec{r}, \vec{r}') \vec{f}_n(\vec{r}') dS' dS \quad (40)$$

$$[\mathbf{L}_q]_{mn} = - \iint \nabla \cdot \vec{f}_m(\vec{r}) \iint h_n(\vec{r}') G(\vec{r}, \vec{r}') dS' dS \quad (41)$$

$$[\mathbf{D}_J]_{mn} = \iint h_m(\vec{r}) \iint G(\vec{r}, \vec{r}') \nabla \cdot \vec{f}_n(\vec{r}') dS' dS \quad (42)$$

$$[\mathbf{D}_q]_{mn} = \iint h_m(\vec{r}) \iint G(\vec{r}, \vec{r}') h_n(\vec{r}') dS' dS \quad (43)$$

$$[\mathbf{Q}]_{mn} = \iint \nabla \cdot \vec{f}_m^b(\vec{r}) \iint \nabla G(\vec{r}, \vec{r}') \cdot (\hat{n} \times \vec{f}_n(\vec{r}')) dS' dS \quad (44)$$

$$[\mathbf{N}_q]_{mn} = \begin{cases} 1, & T_n \in \text{object } m \\ 0, & \text{elsewhere} \end{cases} \quad (45)$$

$$[\mathbf{b}_{tE}]_m = \iint \vec{f}_m(\vec{r}) \cdot \vec{E}^{inc}(\vec{r}) dS \quad (46)$$

$$[\mathbf{b}_{nH}]_m = \iint \nabla \cdot \vec{f}_m^b(\vec{r}) \hat{n} \cdot \vec{H}^{inc}(\vec{r}) dS \quad (47)$$

All constituent elements of the AEFIEH-S have now been defined, except for \mathbf{q}_0 which needs to be solved beforehand to complete the formulation. The solution of the static charges and, indirectly, solution of capacitance extraction problems using AEFIEH-S' static charge solution mechanism, which is henceforth termed static-EFIE(S-EFIE), is the focus of this thesis with an emphasis on closely-spaced geometries with high aspect ratios. S-EFIE is coupled with another formulation termed conductance and capacitance (GC) solver.

2.2 S-EFIE Formulation

The S-EFIE formulation has its physical premise on expression (24). In capacitive problems, there is no incident electric field stimulus. However, in the case of PEC, the boundary condition is such that the scattered and incident electric field cancel each other. Hence, the expression is rewritten as

$$-c \hat{n} \times \iint \rho_0(\vec{r}') \nabla G_0(\vec{r}, \vec{r}') dS' = \frac{1}{\eta} \hat{n} \times \vec{E}_0^{scat}(\vec{r}) \quad (48)$$

This expression can be adapted to capacitive problems by adding a feed to the geometry and applying a delta gap source [12] at the feed. The scattered electric field shall equal the delta gap

source and when tested with a weighting function yield a voltage equivalent to the intended stimulus voltage for the capacitive problem. For the choice of testing function, star function [13], used in S-EFIE, we have

$$\vec{E}_0^{scat}(\vec{r}) = -\delta(\vec{r} - \vec{r}_\delta)V_\delta \quad (49)$$

where V_δ is the intended input voltage at the feed and \vec{r}_δ is the position vector where the input voltage is intended to be enforced, this should be an internal edge in the context of S-EFIE.

The method of moment is used and the subject geometry is approximated with a mesh of N_t triangles with each triangle denoted as T_n where $n = 1, 2, \dots, N_t$. The static charge densities are approximated by a summation of subdomain pulse basis functions as in expressions (32) and (33). The choice of weighting function in this case, however, is chosen to be the star function which are based on RWG functions.

The star test function is defined for every triangle and is the sum of the RWG functions that the subject triangle is associated with, but with the RWG functions divided by their corresponding edge length and their orientation changed so that the subject triangle is the positive triangle in the RWG triangle pair. By this definition, the star function, $\vec{F}_n(\vec{r})$, associated with T_4 in Figure 3 is as follows:

$$\vec{F}_4(\vec{r}) = -\frac{\vec{f}_1(\vec{r})}{e_1} + \frac{\vec{f}_2(\vec{r})}{e_2} + \frac{\vec{f}_3(\vec{r})}{e_3}$$

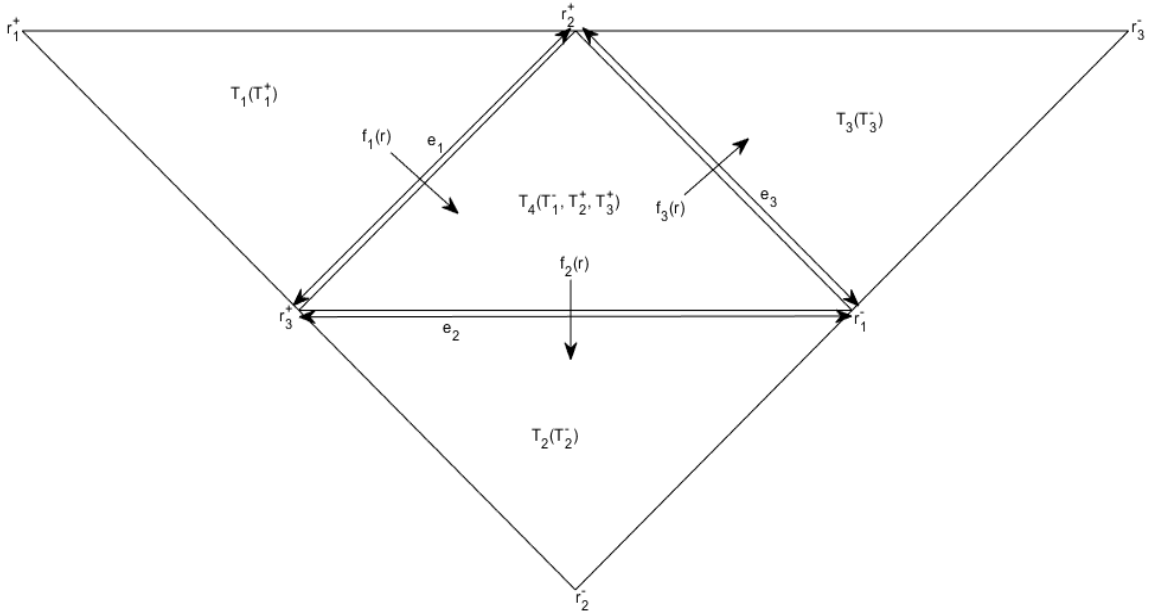


Figure 3: r_1^+ and r_1^- are the free vertices of $f_1(r)$ and T_1^+ and T_1^- are the positive and negative triangle cells of $f_1(r)$. The same naming convention is used for $f_2(r)$ and $f_3(r)$.

Using the testing procedure in expression (35), the following expression is arrived at

$$\begin{aligned}
& - \iint (\hat{\mathbf{n}} \times \vec{F}_m(\vec{r})) \cdot \hat{\mathbf{n}} \times \nabla \iint G_0(\vec{r}, \vec{r}') \sum_{n=1}^{N_t} c q_{0n} h_n(\vec{r}') dS' dS \\
& = \eta^{-1} \iint (\hat{\mathbf{n}} \times \vec{F}_m(\vec{r})) \cdot (\hat{\mathbf{n}} \times \vec{E}_\delta(\vec{r})) dS \\
& - \iint \vec{F}_m(\vec{r}) \cdot \nabla \iint G_0(\vec{r}, \vec{r}') \sum_{n=1}^{N_t} c q_{0n} h_n(\vec{r}') dS' dS = \eta^{-1} \iint \vec{F}_m(\vec{r}) \cdot \vec{E}_\delta(\vec{r}) dS \quad (50)
\end{aligned}$$

After using the vector identity $\nabla \cdot (\psi \mathbf{A}) = \nabla \psi \cdot \mathbf{A} + \psi \nabla \cdot \mathbf{A}$ on (50):

$$\begin{aligned}
& \iint \nabla \cdot \vec{F}_m(\vec{r}) \iint G_0(\vec{r}, \vec{r}') \sum_{n=1}^{N_t} c q_{0n} h_n(\vec{r}') dS' dS \\
& - \iint \iint \nabla \cdot (\vec{F}_m(\vec{r}) G_0(\vec{r}, \vec{r}')) \sum_{n=1}^{N_t} c q_{0n} h_n(\vec{r}') dS' dS \\
& = \eta^{-1} \iint \vec{F}_m(\vec{r}) \cdot \vec{E}_\delta(\vec{r}) dS
\end{aligned}$$

The second term on the left-hand side evaluates to 0 by virtue of the nature of the divergence of RWGs (i.e. the divergence of a RWG is 0 for the triangle pair) which also applies to the star function. Thus, the formulation for the system matrix after testing is

$$\begin{aligned}
& \iint \nabla \cdot \vec{F}_m(\vec{r}) \iint G_0(\vec{r}, \vec{r}') \sum_{n=1}^{N_t} c q_{0n} h_n(\vec{r}') dS' dS = \eta^{-1} \iint \vec{F}_m(\vec{r}) \cdot \vec{E}_\delta(\vec{r}) dS \\
& c \sum_{n=1}^{N_t} q_{0n} \iint \nabla \cdot \vec{F}_m(\vec{r}) \iint G_0(\vec{r}, \vec{r}') h_n(\vec{r}') dS' dS = \eta^{-1} \iint \vec{F}_m(\vec{r}) \cdot \vec{E}_\delta(\vec{r}) dS \quad (51)
\end{aligned}$$

However, this is not complete as the formulation when used, as it is, to construct a system matrix leaves a non-trivial nullspace yielding non-unique solutions to q_n . This has been explained for EFIE tested with RWG test functions [6]. The same applies in this context as well. After the fact that RWG function divergence is triangle-wise constant (i.e. it is constant on the positive and negative triangles), the fact that the basis functions are constant throughout the source triangle, and that each neighboring test triangle pairs have an RWG in their star test function that negate each other, one can see that the possibility for a non-trivial solution to the system matrix exists. If the same logic from Chew and Zhou [6] was applied in this case, then the incidence matrix, \mathbf{D} , is square and will be defined as follows to conform with star functions:

$$[\mathbf{D}]_{mn} = \begin{cases} -1, & \text{Triangle } m \text{ is negative part of star } n\text{'s constituent RWG} \\ 1, 2, 3, & \text{Triangle } m = n. \text{ Value is the number of } n\text{'s internal edges} \\ 0, & \text{Triangle } m \text{ is not part of star } n \end{cases} \quad (52)$$

It can be seen that a vector of 1s is also in the nullspace of \mathbf{D}^T . In order to resolve the problem of the nullspace, a charge neutrality constraint is introduced into the system matrix for each electrically isolated surface and takes the same form as (45). The excitation vector also has the same number of 0s as charge neutrality constraints appended. Thus, the final system of equations in matrix form is

$$\begin{bmatrix} c\mathbf{L}_{q0} \\ \mathbf{N}_q \end{bmatrix} [\mathbf{q}_0] = \eta^{-1} \begin{bmatrix} \mathbf{b}_{tE0} \\ \mathbf{0} \end{bmatrix} \quad (53)$$

where \mathbf{L}_{q0} is a $N_t \times N_t$ matrix, and \mathbf{b}_{tE0} is a $N_t \times 1$ vector and the matrix elements have the following definitions

$$[\mathbf{L}_{q0}]_{mn} = \iint \nabla \cdot \vec{F}_m(\vec{r}) \iint G_0(\vec{r}, \vec{r}') h_n(\vec{r}') dS' dS \quad (54)$$

$$[\mathbf{b}_{tE0}]_m = \iint \vec{F}_m(\vec{r}) \cdot \vec{E}_\delta(\vec{r}) dS \quad (55)$$

This defines the S-EFIE formulation.

2.3 GC Solver Formulation

Consider the potential difference that's constructed by a point charge at the origin. By Coulomb's Law,

$$\vec{F}(\vec{r}) = \frac{q_0 \text{ test } q_0}{4\pi\epsilon r^2} \hat{r} \quad (56)$$

$$\vec{E}(\vec{r}) = \frac{q_0}{4\pi\epsilon r^2} \hat{r} \quad (57)$$

where r is the radial distance between point \vec{r} and q at the origin. The potential difference at \vec{r}_a relative to point \vec{r}_b in the presence of a point charge q at the origin is defined as

$$V(\vec{r}_a)_{\vec{r}_b} = - \int_{\vec{r}_b}^{\vec{r}_a} \vec{E}(\vec{r}) \cdot d\vec{r}$$

Note that because $\vec{E}(\vec{r})$ is directed radially away from the positive point charge or radially inward, if the point charge is negative, only the radial component of the displacement between \vec{r}_a and \vec{r}_b will contribute to the inner product. Therefore,

$$V(\vec{r}_a)_{\vec{r}_b} = - \int_{\vec{r}_b}^{\vec{r}_a} E(\vec{r}) \hat{r} \cdot dr \hat{r}$$

$$\begin{aligned}
&= - \int_{\vec{r}_b}^{\vec{r}_a} \frac{q_0}{4\pi\epsilon r^2} dr \\
&= \frac{q_0}{4\pi\epsilon r} \Big|_{\vec{r}_b}^{\vec{r}_a} \\
&= \frac{q_0}{4\pi\epsilon r_a} - \frac{q_0}{4\pi\epsilon r_b}
\end{aligned}$$

If $r_b \rightarrow \infty$, i.e. potential difference, $V(\vec{r}_a)_{\vec{r}_b}$, is now defined as the energy to move a unit charge from infinite distance to \vec{r}_a , then

$$V(\vec{r}_a)_{\vec{r}_b} = \frac{q_0}{4\pi\epsilon r_a}$$

which we henceforth generalize \vec{r}_a to \vec{r} and denote as

$$V(\vec{r}) = \frac{q_0}{4\pi\epsilon r}$$

When the point charge is removed from the origin, $r = |\vec{r} - \vec{r}'|$ where \vec{r}' is the position vector of the point charge q_0 .

$$V(\vec{r}) = \frac{q_0}{4\pi\epsilon |\vec{r} - \vec{r}'|} \quad (58)$$

If, rather than a point charge, a distribution of charges on a surface is present, then (58) can be modified to the following surface integral to account for the contribution of all the charges in the distribution on the potential difference at \vec{r}

$$\begin{aligned}
V(\vec{r}) &= \iint \frac{\rho_0(\vec{r}')}{4\pi\epsilon |\vec{r} - \vec{r}'|} dS' \\
&= \frac{1}{\epsilon} \iint \rho_0(\vec{r}') G_0(\vec{r}, \vec{r}') dS'
\end{aligned} \quad (59)$$

where $\rho_0(\vec{r}')$ is a surface charge density distribution function in (59).

The object is to solve $\rho_0(\vec{r}')$. The same discretization method is employed in this case in that the geometry is approximated by triangles and subdomain pulse basis functions as in expressions (32) and (33) are used to approximate $\rho_0(\vec{r}')$. The system matrix is formed by substituting (33) into (59) and testing the resulting expression with N_t linearly independent weighting functions to form a system of N_t equations with N_t unknowns or degrees of freedom (DOFs). In accordance with Galerkin's method, the weighting functions shall be the same as the basis functions. The result is

$$\frac{1}{\epsilon} \iint h_m(\vec{r}) \iint G_0(\vec{r}, \vec{r}') \sum_{n=1}^{N_t} q_{0n} h_n(\vec{r}') dS' dS = \iint h_m(\vec{r}) V(\vec{r}) dS$$

$$\frac{1}{\varepsilon} \sum_{n=1}^{N_t} q_{0n} \iint h_m(\vec{r}) \iint G_0(\vec{r}, \vec{r}') h_n(\vec{r}') dS' dS = \iint h_m(\vec{r}) V(\vec{r}) dS \quad (60)$$

$$\frac{1}{\varepsilon} [\mathbf{Z}][\mathbf{q}_0] = \mathbf{V} \quad (61)$$

where \mathbf{Z} is a $N_t \times N_t$ matrix and \mathbf{V} is a $N_t \times 1$ vector with the following definitions

$$[\mathbf{Z}]_{mn} = \iint h_m(\vec{r}) \iint G_0(\vec{r}, \vec{r}') h_n(\vec{r}') dS' dS \quad (62)$$

$$[\mathbf{V}]_m = \iint h_m(\vec{r}) V(\vec{r}) dS \quad (63)$$

This constitutes the GC formulation.

2.4 Numerical Evaluation Methods

The choice of geometry for the study was chosen to be parallel square plate capacitors with very small spatial separation and high aspect ratios, which in this context is defined as the ratio of the largest plate dimension to the separation space between the plates. The aspect ratios that were studied were 5000 or greater.

Generally, quadrature evaluations of surface area for triangles that do not overlap are performed using Gaussian quadrature for triangles and for self-interactions (i.e. the source and field triangles are the same) Duffy transforms [14] are used to evaluate the same. Immediately the challenge at hand was quadrature evaluation convergence.

For example, it was found that in excess of 99.6% of adaptive quadrature evaluation computations for 1 field triangle in a 900-patch parallel plate capacitor with dimensions $10\text{m} \times 10\text{m} \times 0.15\text{m}$ were directed at computing interactions with itself, source triangles that are neighbors sharing an edge or its translational image across the separation space and its image's adjacent neighbors.

This is largely attributable to the singularity in the Green's function. As the distance between the field point and source triangle diminishes, successive adaptive quadrature evaluations tend to show large differences and hence force more quadrature evaluations.

Two methods were used to mitigate this problem. One uses potential integrals [15] for uniform and linear source distributions on polygonal and polyhedral domains. This method, however, is limited to static cases only. The second method is termed extended Duffy transform [16], which, in summary, extends the Duffy transform usage from only being applied to self-interaction quadrature evaluations to include interactions between field triangle points and source triangles where the projected distance of the field point on the source triangle plane is within a given tolerance.

2.4.1 Potential Integrals

The expressions (54) and (62) have integrands that are of the form

$$\iint \frac{1}{R} dS' \quad (64)$$

due to the static Green's function. The potential integrals method makes use of the divergence theorem to reduce the surface integral into a contour integral that is analytical in the limit that the field point, in the case of self-interaction, is confined to an area that approaches zero.

In this thesis' context, the analytical formulation makes use of a 2-dimensional coordinate system that is local to each edge of the source triangle to enable its use in computation. The following parameters (magnitudes and vectors) are defined in Table 1 for each edge of the source triangle in relation to the field point:

Table 1: Definitions of parameters in the local coordinate system defined for each source triangle edge and the field point.

Parameter	Definition
\hat{P}_i^0	A unit vector in the source triangle plane that is perpendicular to edge i or its extension that originates from the field point's projected image on the source triangle plane and terminates at a point on edge i or its extension.
\hat{u}_i	A unit vector in the source triangle plane that is perpendicular to edge i and directed outside of the source triangle.
P_i^0	The line in the source triangle plane that is perpendicular to edge i or its extension and joins the field point's projected image on the source triangle plane to a point on edge i or its extension. This line forms an axis of edge i 's local coordinate system in relation to the field point. Edge i and its extension is the other orthogonal axis in this local coordinate system. P_i^0 also denotes the magnitude of this line.
R_i^+	The distance between the field point and the terminal point of edge i , where the initial and terminal points are determined in a right-handed sense in relation to the source triangle plane's normal vector.
R_i^-	The distance between the field point and the initial point of edge i , where the initial and terminal points are determined in a right-handed sense in relation to the source triangle plane's normal vector.
l_i^+	The position of the terminal point of edge i on a coordinate axis with origin at the intersection of P_i^0 and edge i or its extension. The positive direction of this axis points from the initial point to the terminal point of edge i .
l_i^-	The position of the initial point of edge i on a coordinate axis with origin at the intersection of P_i^0 and edge i or its extension. The positive direction of this axis points from the initial point to the terminal point of edge i .
d	The distance between the field point and its projected image on the source triangle plane.
R_i^0	The distance between the field point and the origin of the local coordinate system. i.e. $R_i^0 = \sqrt{P_i^{02} + d^2}$

Figure 4, Figure 5, and Figure 6 illustrate the local coordinate systems for the 3 edges of a source triangle from a 2-dimensional view with the normal of the source triangle plane in the positive \hat{z} direction.

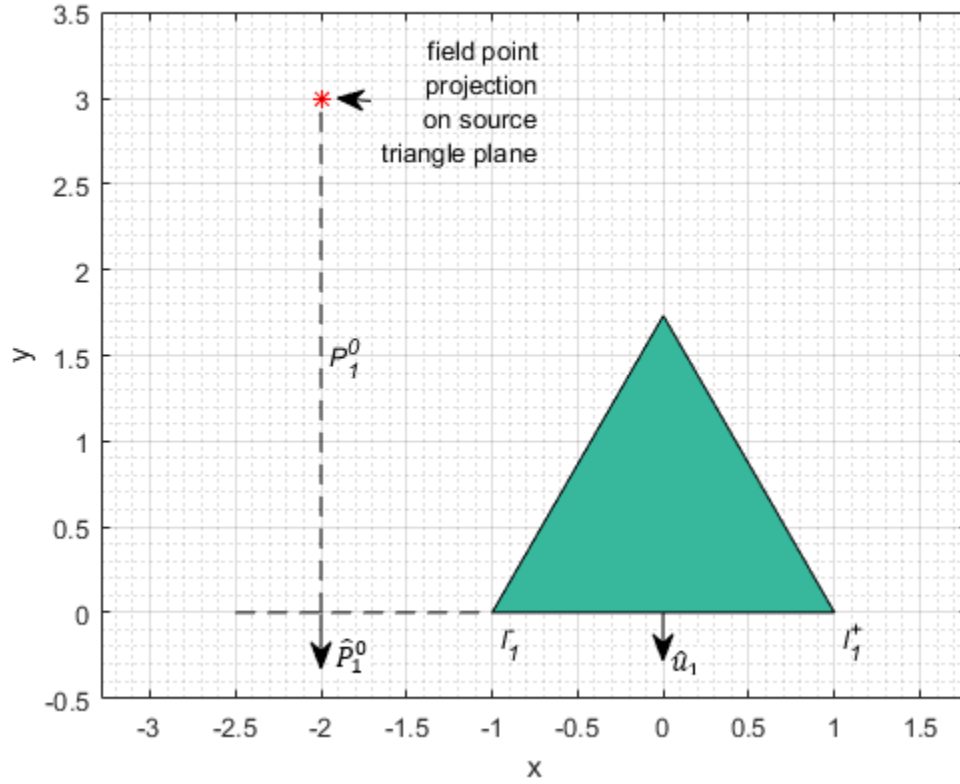


Figure 4: Local coordinate system of edge 1 in relation to the field point projection onto the source triangle plane, which normal is in the z direction.

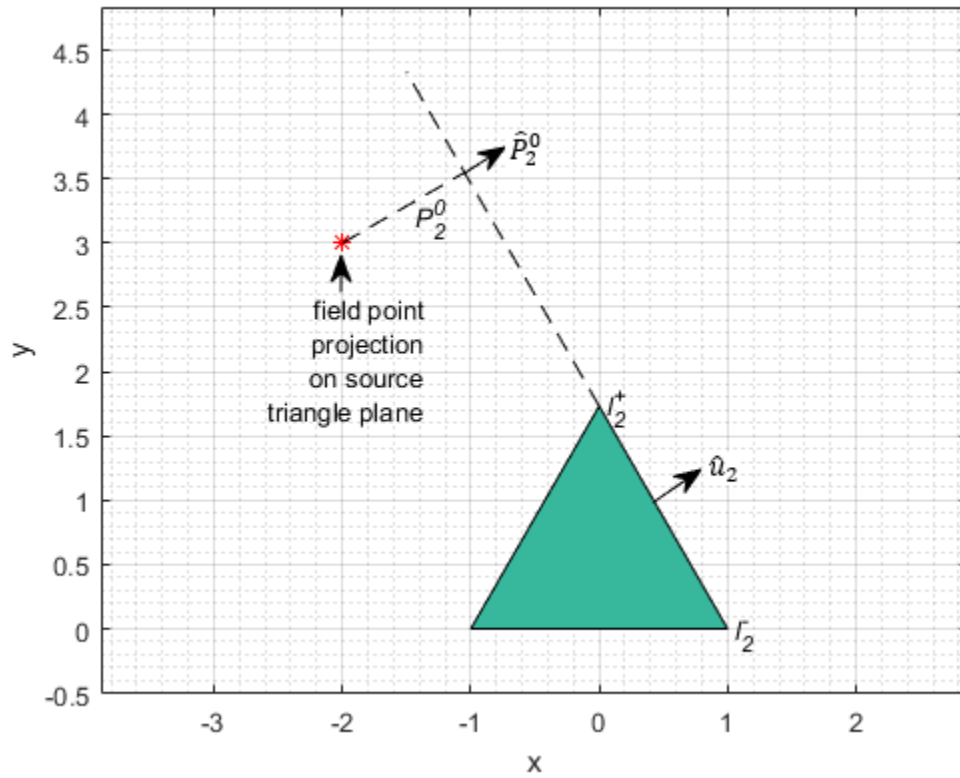


Figure 5: Local coordinate system of edge 2 in relation to the field point projection onto the source triangle plane, which normal is in the z direction.

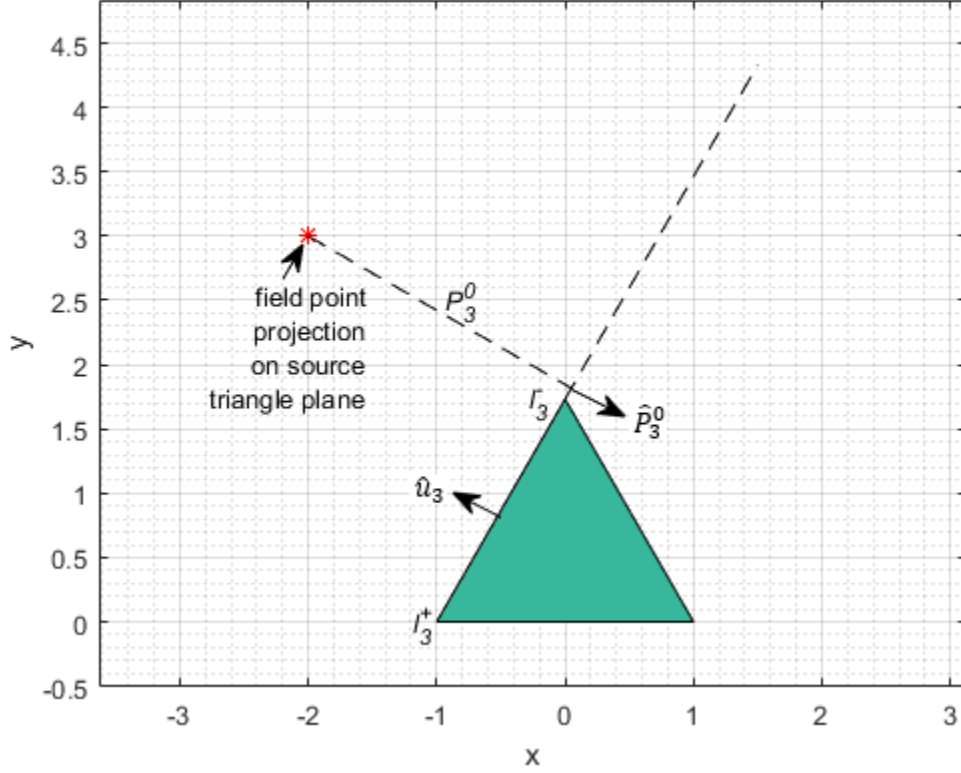


Figure 6: Local coordinate system of edge 3 in relation to the field point projection onto the source triangle plane, which normal is in the z direction.

With these parameters defined, (64) can be analytically evaluated as follows:

$$\iint \frac{1}{R} dS' = \sum_{i=1}^3 \hat{P}_i^0 \cdot \hat{u}_i \left(P_i^0 \ln \frac{R_i^+ + l_i^+}{R_i^- + l_i^-} - |d| \left(\tan^{-1} \frac{P_i^0 l_i^+}{R_i^{0^2} + |d|R_i^+} - \tan^{-1} \frac{P_i^0 l_i^-}{R_i^{0^2} + |d|R_i^-} \right) \right) \quad (65)$$

Note that if the Green's function was dynamic, then potential integrals would not work. However, for capacitive extraction problems where it is static, this method is highly scalable and precludes the need to perform adaptive quadratures on the source triangle, thus, translating into computational savings.

2.4.2 Extended Duffy Transform

The Duffy transform seeks to eliminate the singularity in integrals of the following kind:

$$\int_0^1 \int_0^{x'} \frac{f(x', y')}{\sqrt{x'^2 + y'^2}} dy' dx' \quad (66)$$

The domain of integration is a right triangle in the x' - y' plane. By parametrization:

$$s = x' \quad (67)$$

$$t = \frac{y'}{x'} \quad (68)$$

Thus, (66) becomes:

$$\int_0^1 \int_0^1 \frac{f(s, st)}{\sqrt{s^2 + (st)^2}} s \, dt ds = \int_0^1 \int_0^1 \frac{f(s, st)}{\sqrt{1 + t^2}} dt ds \quad (69)$$

which is no longer singular. Hence, allowing faster convergence. (69) can be computed using Gaussian quadrature for quadrilaterals on a reference plane and then transformed back to the original plane by multiplication with Jacobians linking the plane coordinate systems. This transformation maps a trilateral into a quadrilateral.

The process of using Duffy transforms in quadrature evaluation begins with mapping the source triangle from the global 3-dimensional coordinate system, to a local 2-dimensional coordinate system where the vertices of the source triangle are mapped into vertices with coordinates (0,0), (1,0), and (0,1) assuming a right-handed orientation and the normal of the surface pointing in the positive \hat{z} direction. The source triangle is now a right triangle in the local coordinate system. The Jacobian that maps from the local coordinate system to global coordinate system is twice the area of the source triangle in the global coordinate system. The global coordinates can be mapped into the local coordinates using normalized area coordinates [10] as follows with reference to Figure 7:

$$o_\epsilon = \frac{A_{ONL}}{A_{LMN}} \quad (70)$$

$$o_\eta = \frac{A_{OLM}}{A_{LMN}} \quad (71)$$

$$\vec{O} = (1 - o_\epsilon - o_\eta)\vec{L} + o_\epsilon\vec{M} + o_\eta\vec{N} \quad (72)$$

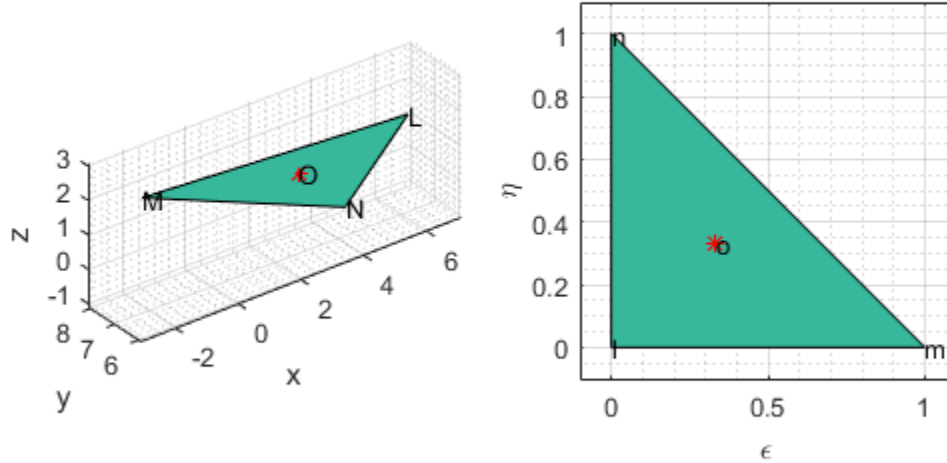


Figure 7: Left is source triangle (LMN) in 3-dimensional global coordinate system and the right is source triangle (lmn) in 2-dimensional local coordinate system. O denotes the field point in global coordinates, o denotes the field point in local coordinates.

Next, the trilateral in the local coordinate system needs to be broken into sub-trilaterals where each trilateral has the field point and 2 of the source trilateral vertices for its vertices. Note that if the field point is a vertex of the source trilateral, then there is only 1 sub-trilateral (the source triangle itself), and if the field point is located on a source trilateral edge, then there are only 2 sub-trilaterals that can be defined. Note that the field point is the point where the quadrature evaluation is singular.

Next each sub-triangle is mapped into a Duffy plane quadrilateral, wherein Gaussian quadrature for quadrilaterals is evaluated. Note that the Jacobian mapping from the Duffy plane to local coordinate plane is dependent on which 2 adjacent vertices of the quadrilateral the field point is mapped to. Points on the Duffy plane can be mapped back to the local coordinate plane using nodal shape functions [17] for quadrilaterals. If the axes of the Duffy plane are labeled s and t (henceforth also known as the s - t plane), then the nodal shape functions and their uses to map back to the local coordinate plane (the ϵ - η plane) are:

$$N_1(s, t) = (1 - s)(1 - t) \quad (73)$$

$$N_2(s, t) = s(1 - t) \quad (74)$$

$$N_3(s, t) = st \quad (75)$$

$$N_4(s, t) = (1 - s)t \quad (76)$$

Using Figure 8 for an example, the mapping will work as follows to define the relationship between an arbitrary point $\vec{p}'(s, t)$ in the s - t plane to $\vec{p}(\epsilon, \eta)$ in the ϵ - η plane:

$$\begin{aligned} p_\epsilon &= N_1 o_\epsilon + N_2 l_\epsilon + N_3 m_\epsilon + N_4 o_\epsilon \\ &= (1 - s)o_\epsilon + s(1 - t)l_\epsilon + stm_\epsilon \\ p_\eta &= N_1 o_\eta + N_2 l_\eta + N_3 m_\eta + N_4 o_\eta \\ &= (1 - s)o_\eta + s(1 - t)l_\eta + stm_\eta \end{aligned}$$

By definition, the Jacobian is defined as:

$$Jac = \begin{vmatrix} \frac{d\epsilon}{ds} & \frac{d\eta}{ds} \\ \frac{d\epsilon}{dt} & \frac{d\eta}{dt} \end{vmatrix} \quad (77)$$

Therefore, the Jacobian mapping from s - t plane to ϵ - η plane in this case

$$\begin{aligned} Jac &= |(-o_\epsilon + (1 - t)l_\epsilon + tm_\epsilon)(-sl_\eta + sm_\eta) \\ &\quad - (-sl_\epsilon + sm_\epsilon)(-o_\eta + (1 - t)l_\eta + tm_\eta)| \end{aligned}$$

The final step is to perform the Gaussian quadrature for quadrilaterals in the Duffy plane and multiply the result by the Jacobians mapping from the Duffy plane to the global coordinates. This needs to be repeated for all the sub-trilaterals and then summed together to get the final result.

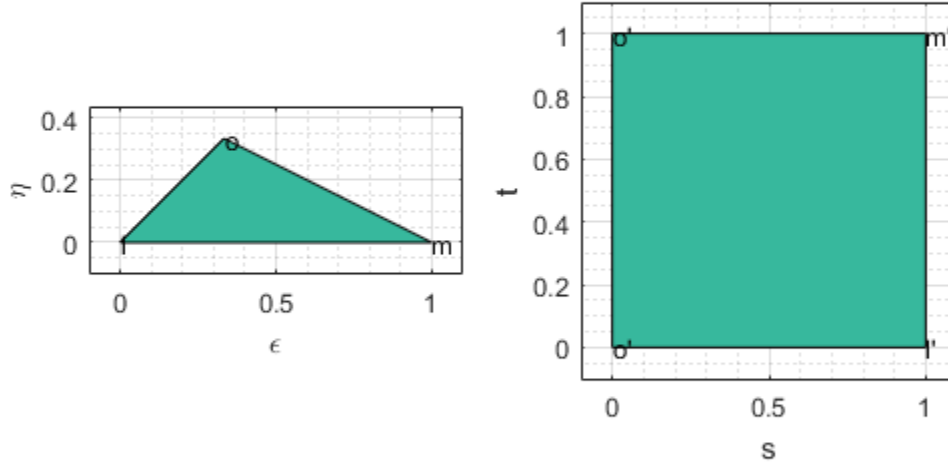


Figure 8: olm in local coordinate plane (left) maps to o'l'm'o' in the Duffy plane (right)

This is in general how the Duffy transform would be performed and used. The extended Duffy transform extends this capability by allowing the field point to lie outside the source triangle. The field point may also not be on the same plane as the source triangle. The vertices of the source triangle are mapped from x - y - z to ϵ - η the same way as the Duffy transform, but the sub-trilaterals cannot be formed if the field point is not on the same plane as the source triangle. Therefore, the field point must be projected onto the source triangle plane. It is for this reason that the ratio of the distance between the field point and its projected image on the source triangle plane to the largest dimension of the source triangle must be within a tolerance. This capability requires that the field point be projected onto the ϵ - η plane accurately. Note that in extended Duffy transform, the field point may lie outside the right triangle in the ϵ - η plane. Also, a scheme must be present to ensure that the summation of the quadrature results of the sub-trilaterals account for the effects of the source triangle only and not any part outside it on the field point.

After the fact that the field point may not be on the same plane as the source triangle, normalized area coordinates and its mapping expressions (70), (71), and (72) between the global and local coordinates are not valid. In this case, a mapping using Dupin coordinates [16] is

proposed. In this approach, the local coordinates are augmented from \mathbb{R}^2 to \mathbb{R}^3 , where the 3rd coordinate is in the direction of the surface's normal and is denoted by symbol ξ . $\xi = 0$ means that the point lies on the plane of the source triangle. Unitary vectors need to be determined. These are essentially vectors that relate the change in the position vector in x - y - z to changes of the same position vector in the ϵ , η , and ξ directions in the local coordinate system. Hence, as an example, the unitary vectors, with reference to Figure 7, are

$$\vec{a}_1 = \frac{d\vec{r}}{d\epsilon} = \vec{r}_M - \vec{r}_L$$

$$\vec{a}_2 = \frac{d\vec{r}}{d\eta} = \vec{r}_N - \vec{r}_L$$

$$\vec{a}_3 = \frac{d\vec{r}}{d\xi} = \vec{a}_1 \times \vec{a}_2$$

If the field point in ϵ - η - ξ is denoted by column vector $[\vec{p}(\epsilon, \eta, \xi)]$ and the corresponding field point in x - y - z is denoted by column vector $[\vec{r}(x, y, z)]$, and \vec{a}_1 , \vec{a}_2 , and \vec{a}_3 are column vectors as well, then

$$\begin{aligned} & [\vec{a}_1 \quad \vec{a}_2 \quad \vec{a}_3]([\vec{p}(\epsilon + \delta_1, \eta + \delta_2, \xi + \delta_3)] - [\vec{p}(\epsilon, \eta, \xi)]) \\ & = [\vec{r}(x + \Delta_1, y + \Delta_2, z + \Delta_3)] - [\vec{r}(x, y, z)] \end{aligned}$$

This suggests that Newton's method may be used to iteratively solve for the field point's mapping in ϵ - η - ξ by achieving the goal of finding the zero of the expression $[\vec{r}(x, y, z)] - [\vec{r}(x + \Delta_1, y + \Delta_2, z + \Delta_3)]$. Thus, the Newton's method expression to use is

$$\begin{aligned} [\vec{p}(\epsilon, \eta, \xi)] & = [\vec{p}(\epsilon + \delta_1, \eta + \delta_2, \xi + \delta_3)] \\ & - [\vec{a}_1 \quad \vec{a}_2 \quad \vec{a}_3]^{-1}([\vec{r}(x, y, z)] - [\vec{r}(x + \Delta_1, y + \Delta_2, z + \Delta_3)]) \end{aligned} \quad (78)$$

Once $\vec{p}(\epsilon, \eta, \xi)$ is found, its ξ coordinate is set to 0. This effectively projects the field point onto the source triangle plane.

The mapped field point in the ϵ - η plane may resemble that in Figure 9. In such a scenario, the sub-trilaterals would be as depicted in Figure 10.

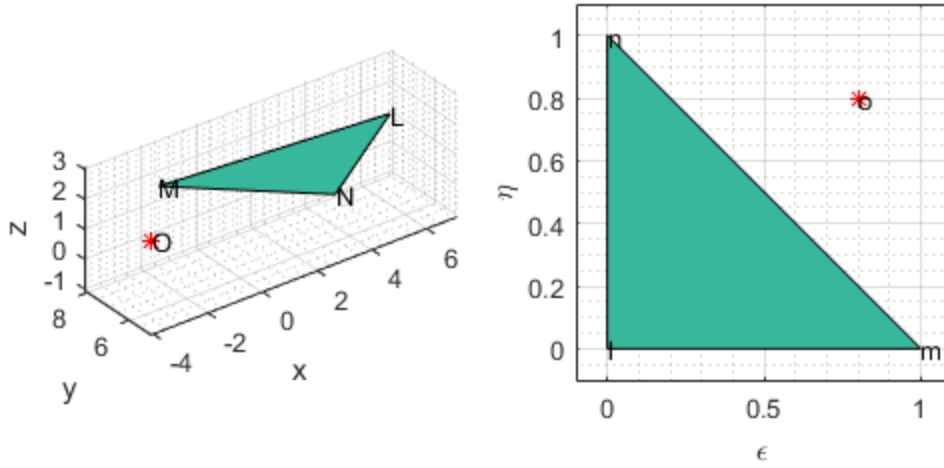


Figure 9: Field point (O) and source triangle (LMN) in global coordinates (left). Field point (o) and source triangle (lmn) in local coordinates (right).

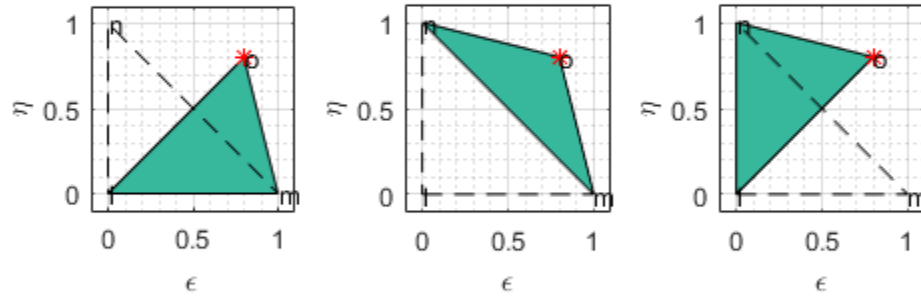


Figure 10: Sub-trilaterals when field point is not in source triangle.

Hence, care needs to be taken when the contributions from the sub-trilaterals are summed. In this example, the correct result comes from adding the contributions from the leftmost and rightmost sub-trilateral and subtracting the contribution from the center sub-trilateral. This complexity can be handled by not taking the absolute value of the Jacobian mapping from the $s-t$ plane to the $\epsilon-\eta$ plane, and adopting a consistent order in mapping the vertices of the sub-trilaterals in a right-handed sense relative to the normal of the source triangle in the $\epsilon-\eta$ plane.

2.5 Effects of Far Interactions

In the course of the investigation, it was found that the geometry under study exhibited an interesting behavior in its system matrix singular value distribution that contributed to high condition numbers for both the S-EFIE and GC solver formulations. As an illustration, Figure 11, a 10m-by-10m parallel square plate capacitor with 0.002m separation with the following meshing where the top and bottom plates have matching cell arrangements.

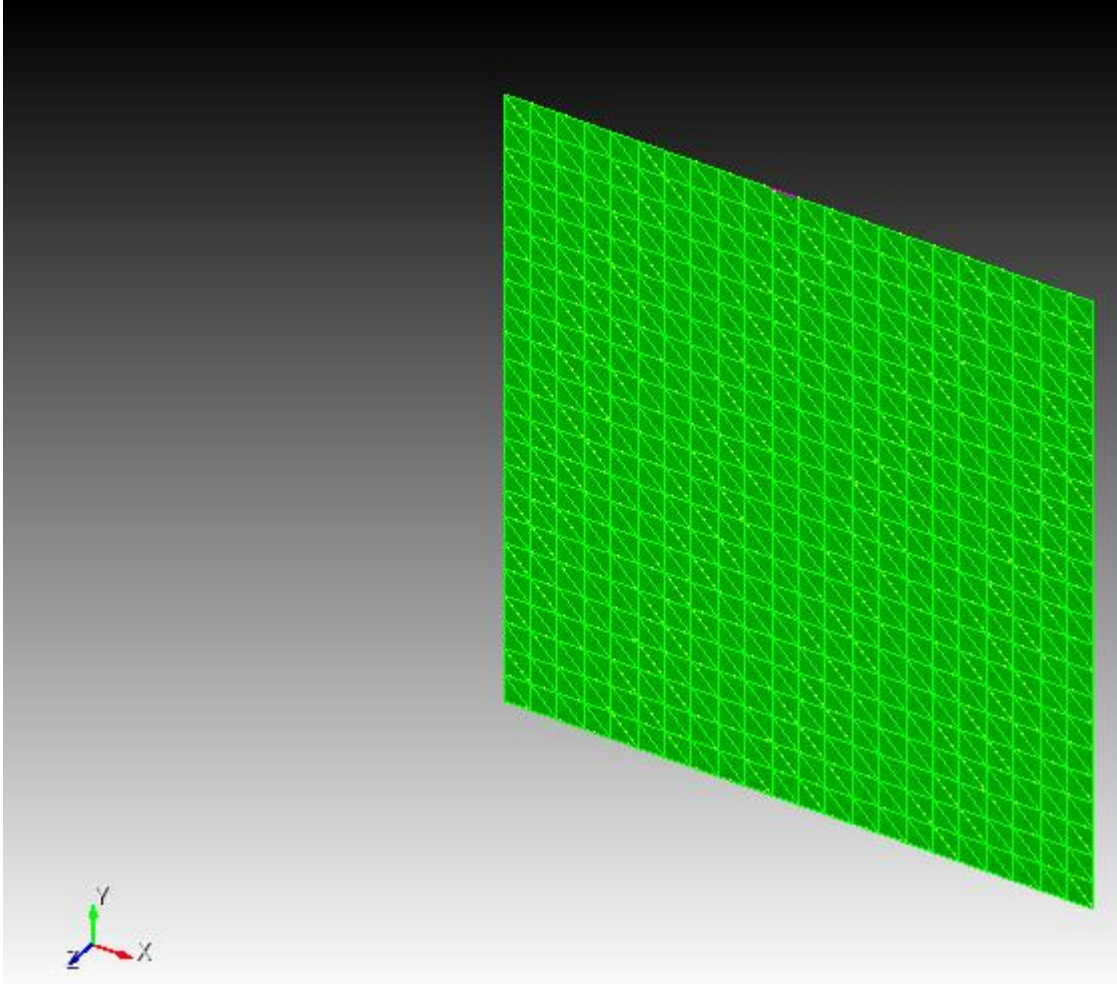


Figure 11: Parallel plate capacitor with dimensions 10m-by-10m with 0.002m plate separation. There are 2028 triangles in the mesh; 1012 triangles on the top and bottom and 4 on the feed between the plates. The bottom and top plates have matching cell arrangements.

The same geometry is used as input to the S-EFIE and GC solver formulations and the singular value distributions were observed. Figure 12 and Figure 13 exhibit the data and show a sudden drop in the middle of the descending order distribution of the singular values.

The hypothesis for the root cause of this behavior is that as the separation between the plates decreases and the aspect ratio of the geometry increases interactions between a field triangle and distant source triangle pairs that are translational images of each other across the separation delta appear to cancel each other. This translates to the system matrix being rank deficient and exhibit high condition numbers. This is largely a problem caused by the physics of the geometry. Hence, to prove this hypothesis, the geometry in Figure 11 is varied by changing the separation delta from 0.002m to 0.02m and then to 0.2m and repeating the formulation

evaluation on each variation and then observing the distribution of the singular values. The results are detailed in Figure 12 and Figure 13 and appear to support this hypothesis.

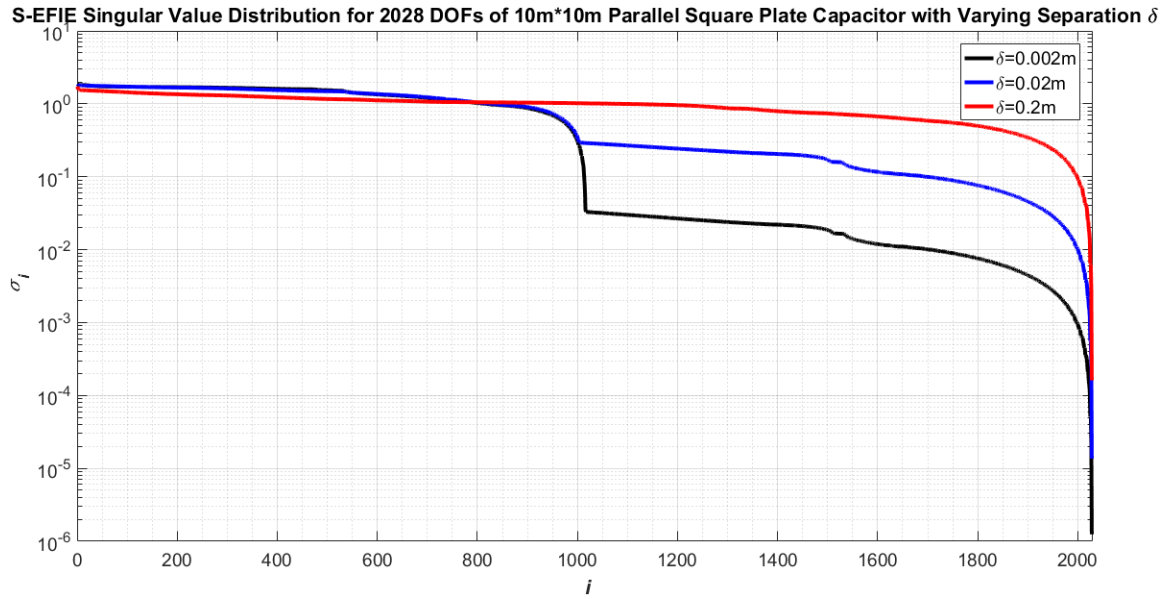


Figure 12: Effects of high aspect ratio and low separation delta between parallel capacitor plates on S-EFIE formulation.

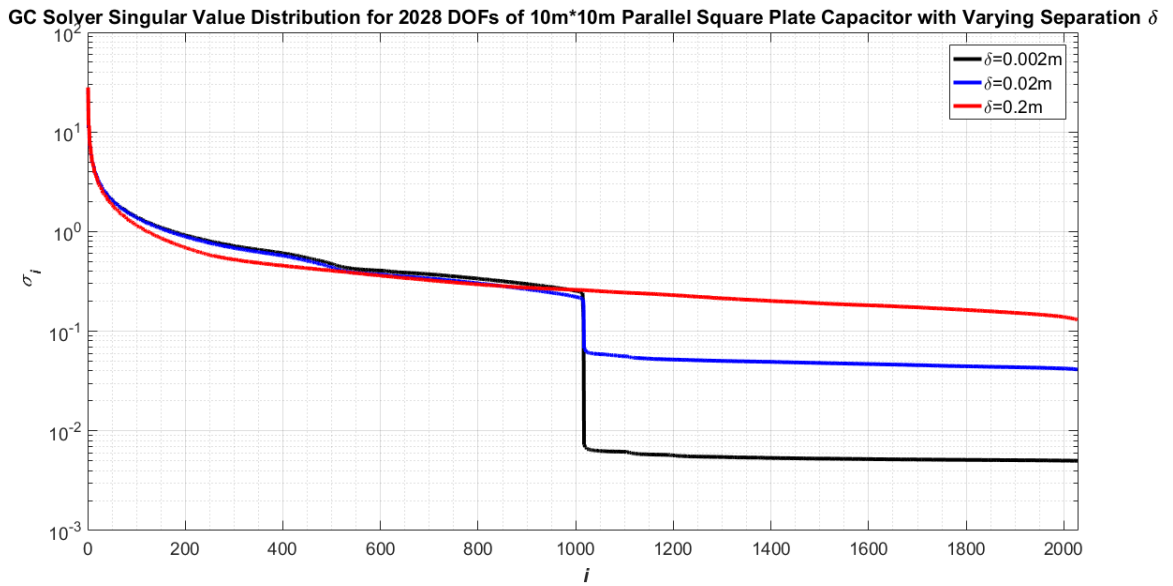


Figure 13: Effects of high aspect ratio and low separation delta between parallel capacitor plates on GC solver formulation.

This observation motivates a preconditioning method that seeks to amplify the differences in interaction between a field triangle and a source triangle and the interaction between the same field triangle and the translational pair of the source triangle across the separation delta. Thus, a simple preconditioning method is tested in a dense fill evaluation of the same geometry (i.e. 10m-by-10m with separation delta 0.002m). In order to facilitate the description of the preconditioning method, Figure 14 shall be used for illustration. T^{Fld} denotes the field triangle, T_{top}^{Src} and T_{bot}^{Src} denote the top and bottom source triangles respectively. The preconditioner adds the interaction of T_{bot}^{Src} with T^{Fld} to the interaction of T_{top}^{Src} with T^{Fld} and subtracts the interaction of T_{top}^{Src} with T^{Fld} from the interaction of T_{bot}^{Src} with T^{Fld} . This effectively means adding the column vector associated with T_{bot}^{Src} to the column associated with T_{top}^{Src} and subtracting the column vector associated with T_{top}^{Src} from the column vector associated with T_{bot}^{Src} in the system matrix. The preconditioned matrix is then iteratively scaled using the diagonal scaling algorithm in [4]. The results of the preconditioned system matrix are shown in Figure 15 and Figure 16.

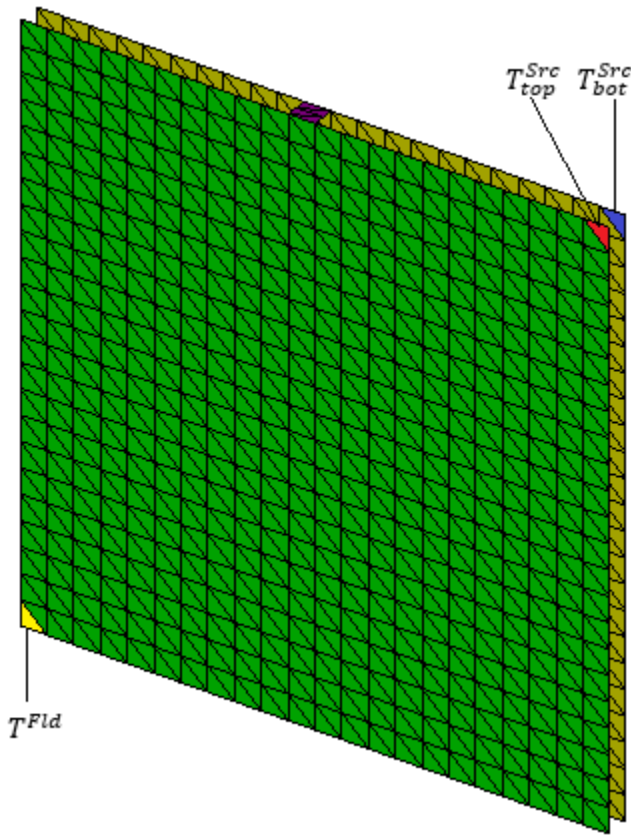


Figure 14: Joint effect of source triangles that are mutual images across the separation delta on a far field triangle.

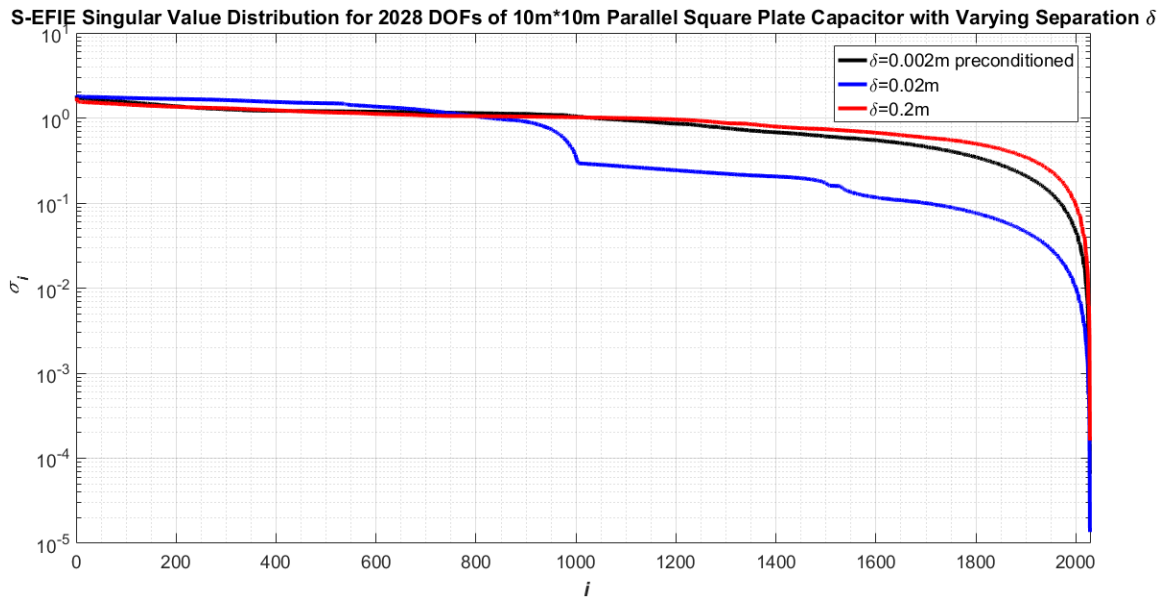


Figure 15: Result of preconditioned S-EFIE system matrix compared to cases of lower aspect ratio.

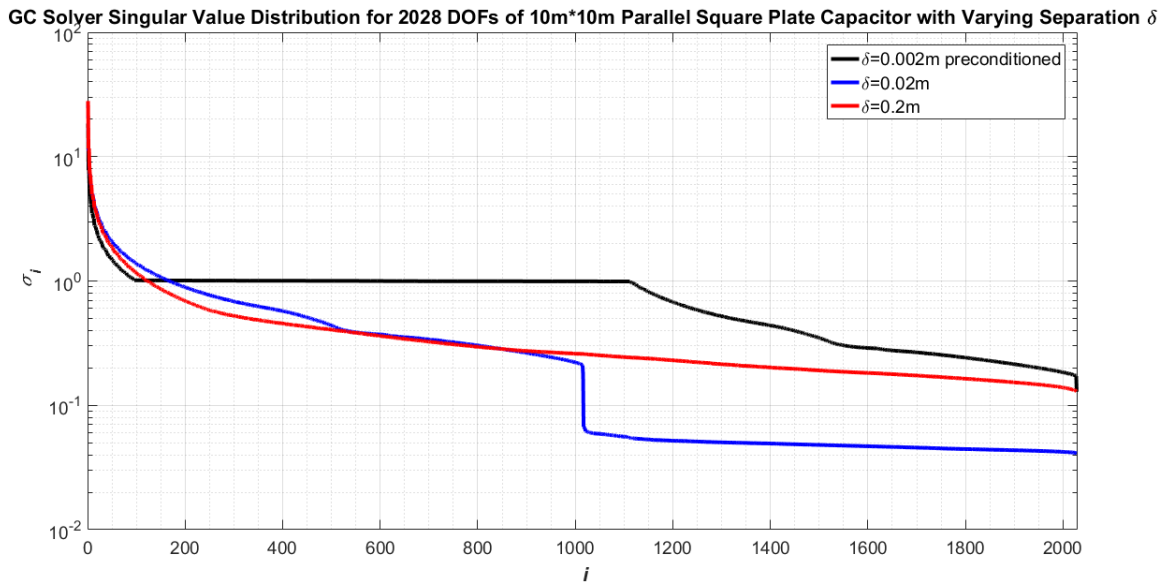


Figure 16: Result of preconditioned GC solver system matrix compared to cases of lower aspect ratio.

Table 2: Condition numbers of S-EFIE and GC solver for 10m-by-10m parallel plate capacitor with 0.002m separation delta and 2028 DOFs.

	S-EFIE	GC Solver
Condition number without preconditioning	1479018.695248549	5180.316405943132
Condition number with preconditioning	27237.43512851236	144.9657994147753

2.6 MFD and LOGOS

MFD makes use of local global solution (LOGOS) [18] modes to factor a system matrix recursively into a sparse matrix. The concept seeks to fit the physical geometry into several grid levels of cuboids in the 3-dimensional case (called an oct-tree), rectangles in the 2-dimensional case (called a quad-tree), or line segments in the 1-dimensional case. The mesh cells are grouped by the grid location that they belong in and their column and row vectors within the system matrix are re-arranged to reflect the same. Based on this re-arranged system matrix, localizing basis functions are found and, with them, projection matrices are found in order to project what remains to be non-localizing basis functions on the current level of the grid to the next level (a coarser grid), where the process is repeated.

A 1-dimensional example shall be used to illustrate the concept. Suppose the subject geometry is a strip and 3 levels of grid is fitted onto the geometry as in Figure 17. At level-3, the triangles, which correspond to DOFs, are grouped into the 4 groups in the level-3 grid. The system matrix is re-arranged to reflect this and the basis functions, denoted by Λ^L , that would give rise to the excitation pattern in Figure 18 are found.

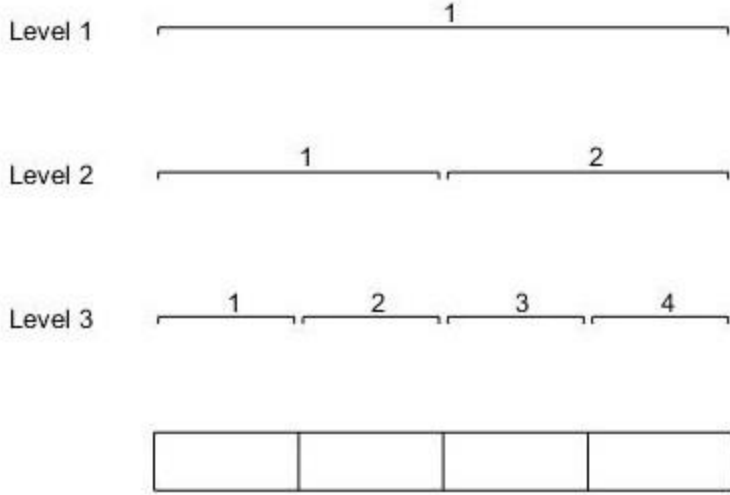


Figure 17: A strip fitted with 3-level grid in MFD LOGOS factorization.

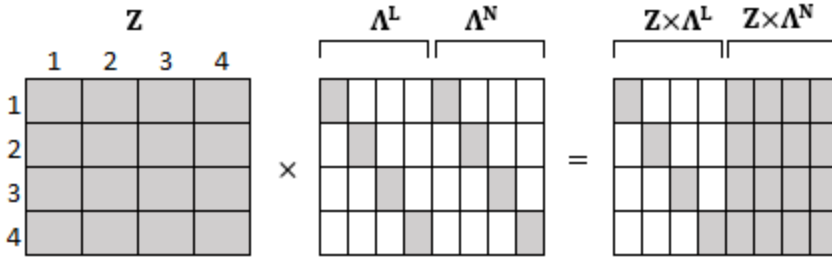


Figure 18: The system matrix rearranged to match the LOGOS grid grouping. Localizing basis functions multiplied with system matrix yield excitation that is localized, non-localizing basis functions when multiplied result in excitation that reach the entire domain.

Starting from the finest level, i.e. level-3, once the localizing (Λ_3^L) and non-localizing (Λ_3^N) basis functions are found and letting $\Lambda_3 = [\Lambda_3^L \quad \Lambda_3^N]$, a projection matrix, $\mathbf{P}_3 = [\mathbf{P}_3^L \quad \mathbf{P}_3^N]$, is found such that expressions (79) and (80) are true:

$$\mathbf{Z} = \mathbf{Z}_3 = \mathbf{P}_3 \hat{\mathbf{Z}}_3 \Lambda_3^{-1} \quad (79)$$

$$\hat{\mathbf{Z}}_3 = \mathbf{P}_3^H \mathbf{Z}_3 \Lambda_3 \approx \begin{bmatrix} \mathbf{I} & (\mathbf{P}_3^L)^H \mathbf{Z}_3 \Lambda_3^N \\ \mathbf{0} & (\mathbf{P}_3^N)^H \mathbf{Z}_3 \Lambda_3^N \end{bmatrix} = \begin{bmatrix} \mathbf{I} & \mathbf{Z}_3^{LN} \\ \mathbf{0} & \mathbf{Z}_3^{NN} \end{bmatrix} \quad (80)$$

This requires that \mathbf{P}_3^L and \mathbf{P}_3^N be mutually orthogonal and that \mathbf{P}_3^L be unitary with respect to $\mathbf{Z}_3 \Lambda_3^L$. Therefore, the convenient method to find \mathbf{P}_3 is to take a QR factorization of $\mathbf{Z}_3 \Lambda_3^L$ and thus resulting in a Q matrix that is constituted from mutually orthogonal column vectors and because of the structure of $\mathbf{Z}_3 \Lambda_3^L$, which is highly localized, the R upper triangular matrix becomes block diagonal instead. \mathbf{P}_3^L will be the Q matrix column vectors that form the basis of the column space

of $Z_3 \Lambda_3^L$, denote as Q_1 , whereas P_3^N will be the remaining Q matrix column vectors, denote as Q_2 . The purpose of the projection matrix is to project the resulting non-localized excitation to a coarser level of grid, level-2 in this discussion, to be factorized in (80) using the same procedure. Such an arrangement while not immediately evident in its usefulness at only 3 levels of grid will become crucial as the subject problem scales up in DOF count and require more grid levels. Figure 19 and Figure 20 illustrate the structure of the matrices. Note that at level-1, no further factorization is possible as the domain of the source and the excitation are in the same group.

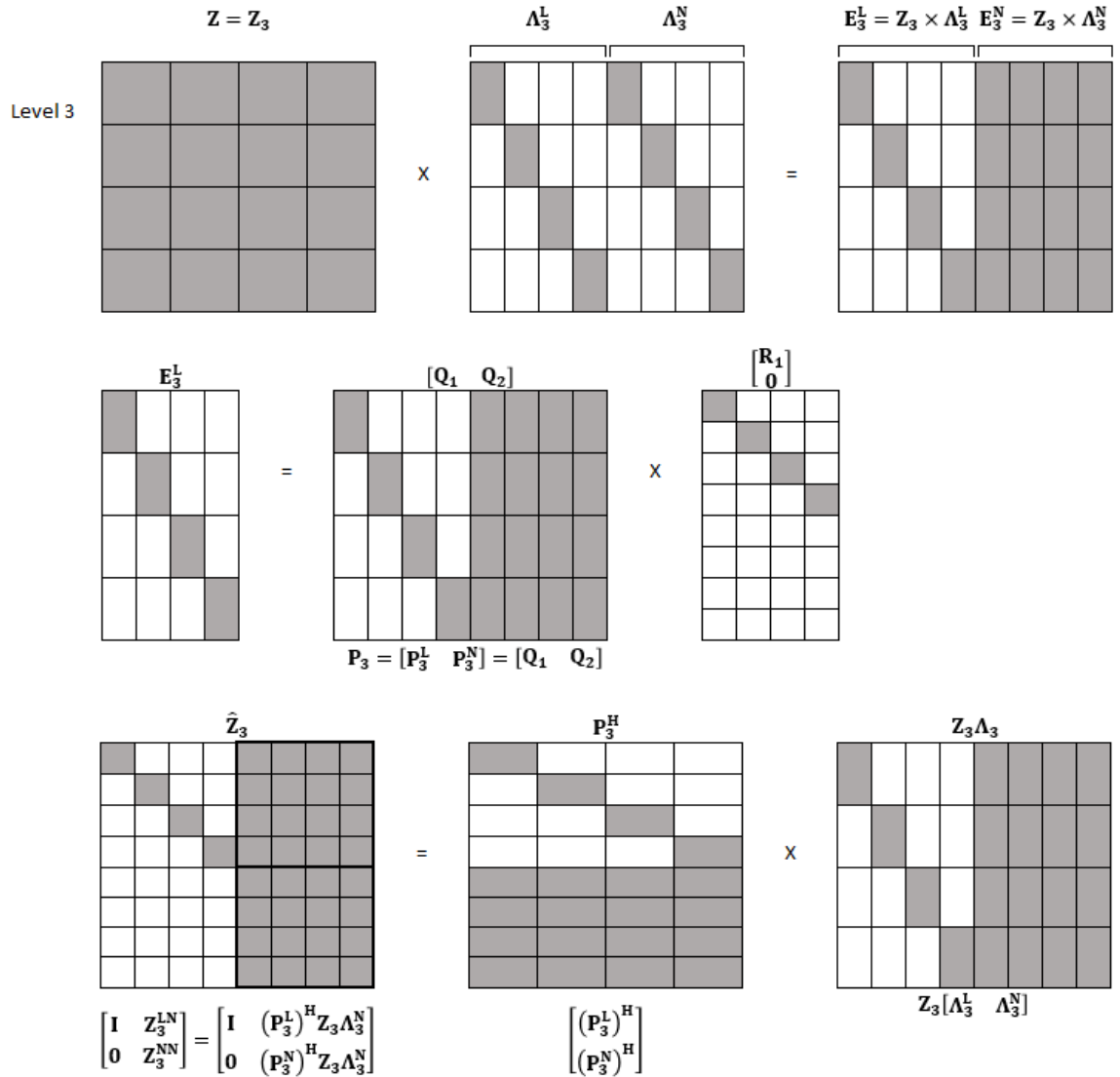


Figure 19: Level-3 factorization matrix structures.

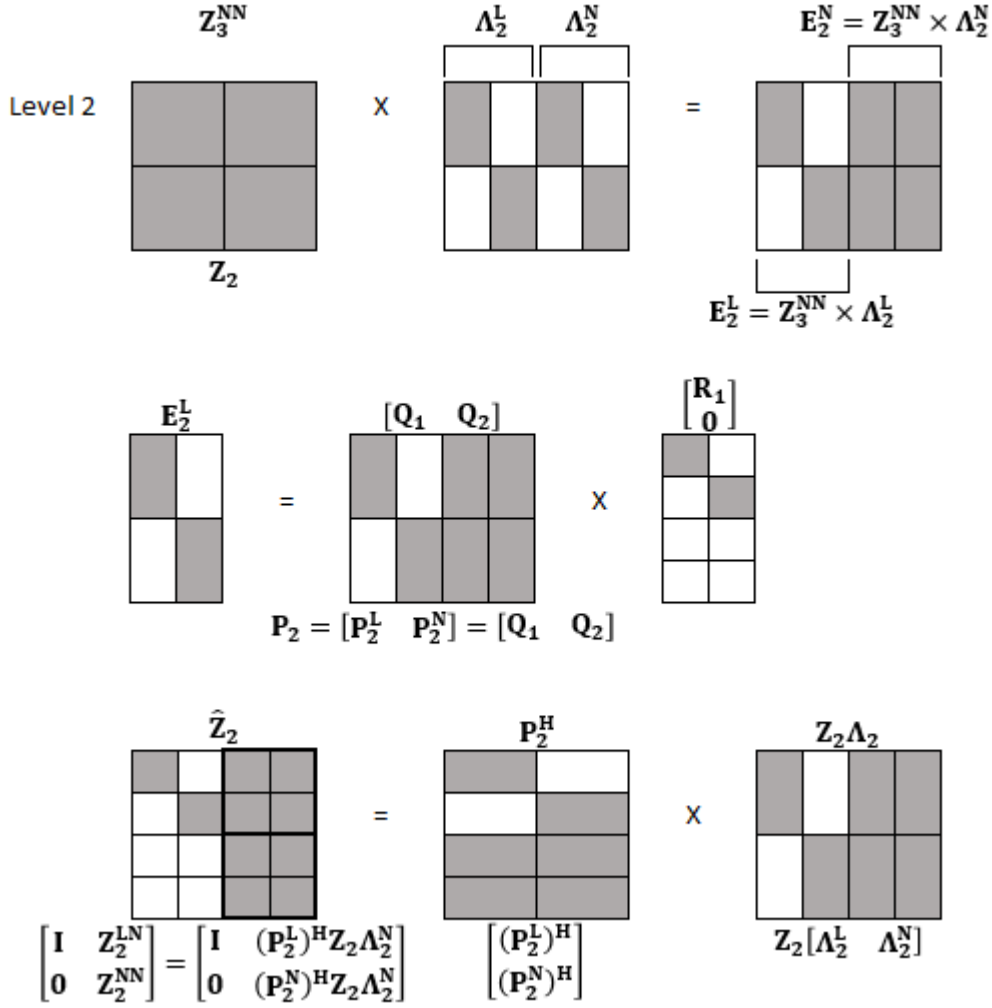


Figure 20: Level-2 factorization matrix structures.

With these constructs in place, the inverse of the system matrix can be found using the following expressions:

$$\mathbf{Z}^{-1} = \Lambda_3 \begin{bmatrix} \mathbf{I} & -\mathbf{Z}_3^{\text{LN}} \\ \mathbf{0} & \mathbf{I} \end{bmatrix} \begin{bmatrix} \mathbf{I} & \mathbf{0} \\ \mathbf{0} & (\mathbf{Z}_3^{\text{NN}})^{-1} \end{bmatrix} \mathbf{P}_3^{\text{H}} \quad (81)$$

where

$$(\mathbf{Z}_3^{\text{NN}})^{-1} = \mathbf{Z}_2^{-1} = \Lambda_2 \begin{bmatrix} \mathbf{I} & -\mathbf{Z}_2^{\text{LN}} \\ \mathbf{0} & \mathbf{I} \end{bmatrix} \begin{bmatrix} \mathbf{I} & \mathbf{0} \\ \mathbf{0} & (\mathbf{Z}_2^{\text{NN}})^{-1} \end{bmatrix} \mathbf{P}_2^{\text{H}} \quad (82)$$

The localizing and non-localizing basis functions can be found using the procedure outlined in [19] and is summarized here. The procedure starts with partitioning the re-arranged system matrix by the column groups. Using the level-3 example in this discussion, the re-arranged system matrix would be partitioned into 4 sub-system matrices where each sub-system matrix has 4 row groups and 1 column group. Each sub-system matrix evaluation yields the

localized and non-localized basis functions associated with the column group denoted $\Lambda_{i(l)}^L$ and $\Lambda_{i(l)}^N$ respectively, where i is the group in grid level- l for both cases. A QR factorization is first performed on the sub-system matrices to yield the \mathbf{Q}_i and \mathbf{R}_i matrices. The sub-matrix within \mathbf{Q}_i that corresponds in location and structure with the self-term in the sub-system matrix is then picked out for a singular value decomposition operation. Due to the fact that column vectors in the \mathbf{Q}_i matrix are mutually orthogonal, the singular values in of the \mathbf{Q}_i sub-matrix will be less than but approaching 1. A tolerance value, ε , is set to shortlist the singular values from which their corresponding V singular vectors will be picked out to constitute a new matrix denoted $\hat{\mathbf{v}}$. The following inequality is used as the criteria to shortlist the singular values:

$$s_j > 1 - 0.5\varepsilon^2 \quad (83)$$

where s_j denote the singular values sorted from maximum to minimum. Once $\hat{\mathbf{v}}$ is determined from the shortlisted singular values, $\lambda_{i(l)}^L$ and $\lambda_{i(l)}^N$ are found by the expressions (84) and (85):

$$\lambda_{i(l)}^L = \mathbf{R}_i^{-1} \hat{\mathbf{v}} \quad (84)$$

$$\lambda_{i(l)}^L = \mathbf{q}\mathbf{r} = [\mathbf{q}_1 \quad \lambda_{i(l)}^N] \begin{bmatrix} \mathbf{r} \\ \mathbf{0} \end{bmatrix} \quad (85)$$

The basis function matrix $\Lambda_{i(l)}^L$ is built by constructing a matrix of zeros with row count equal the sub-system matrix row count and column count equal the column count of $\lambda_{i(l)}^L$ and then substituting $\lambda_{i(l)}^L$ into the rows of the structure that correspond with the self-term in the sub-

system matrix. $\Lambda_{i(l)}^N$ is constructed from $\lambda_{i(l)}^N$ in the same way. Figure 21 summarizes the procedure.

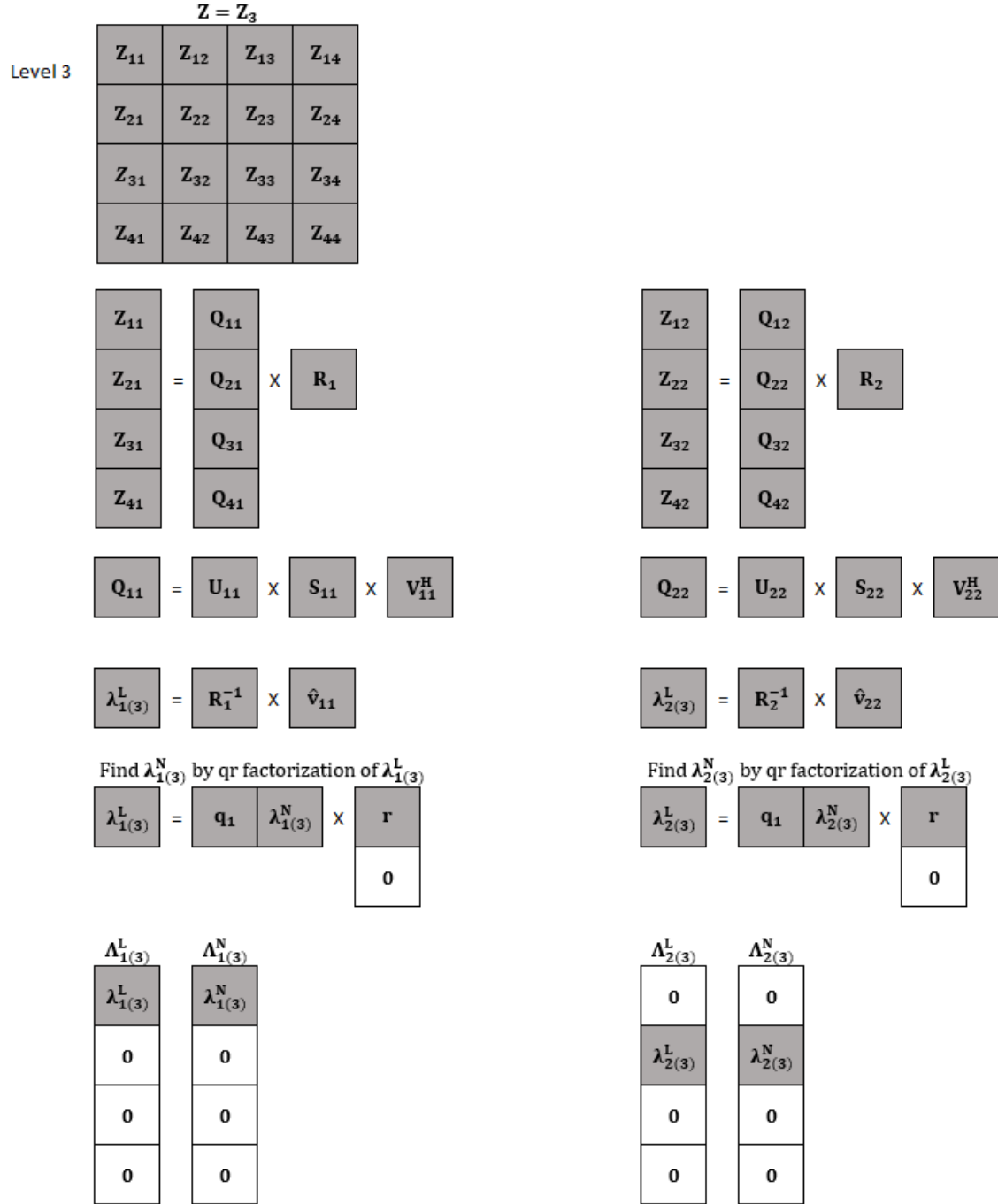


Figure 21: Steps to build the localizing and non-localizing basis function matrices.

While this procedure results in easier system matrix inversion and, thus, shortens solve time for the charge distribution of the problem at hand, the operation to find the localizing basis

functions is an expensive one since it requires seeking orthogonal column vectors spanning the sub-system matrices using QR decomposition. For this reason, MFD exploits a system matrix compression algorithm termed MLSSM [20] along with the Θ R factorization [21] scheme. The reader is referred to the bibliography for the details of the implementation of MLSSM. Briefly, MLSSM represents a re-arranged system matrix, where DOFs that are physically close are grouped together, with the following recursive expression: (assuming a 4-level grid is imposed)

$$\begin{aligned}
Z &= \hat{Z}_4 + U_4 Z_3 V_4^H \\
&= \hat{Z}_4 + U_4 (\hat{Z}_3 + U_3 Z_2 V_3^H) V_4^H \\
&= \hat{Z}_4 + U_4 (\hat{Z}_3 + U_3 (\hat{Z}_2) V_3^H) V_4^H
\end{aligned} \tag{86}$$

In (86), the \hat{Z}_i terms refer to system matrix terms that represent near neighbor interactions in level- i groups. The Z_i terms represent compressed far group interactions in level- $i + 1$. The U_i and V_i^H terms are block diagonal matrices that expand the Z_{i-1} term to have the same row and column dimensions as \hat{Z}_i . The near interaction terms at the finest level groups are filled directly. The far interactions are filled using ACA [22] where an outer product is obtained. The outer product is manipulated to give a form that resembles a SVD form. The fact that ACA is used to perform far interaction fills imply that not all system matrix terms are necessarily present and avoids the need for a dense fill which would have resulted in $O(n^2)$ complexity. The use of MLSSM for compression also translates into savings in memory to contain the system matrix.

Summarily, in order to compute $\lambda_{i(l)}^L$ and then $\Lambda_{i(l)}^L$ requires a QR decomposition of the sub-system matrix to find the upper triangular matrix \mathbf{R}_i and the segment of \mathbf{Q}_i that concerns $\Lambda_{i(l)}^L$. However, if \mathbf{R}_i is available, then the relevant segment of \mathbf{Q}_i can be computed. For example, referring to Figure 21, if \mathbf{R}_1 is known, then \mathbf{Q}_{11} can be found as $\mathbf{Z}_{11} \mathbf{R}_1^{-1}$. The Θ R algorithm makes use of MLSSM's representation of a sub-system matrix. For instance, the sub-system matrix associated with group 1 in level-4 is $Z_{1(4)} = \hat{Z}_{1(4)} + U_4 \hat{Z}_3 V_{1(4)}^H + U_4 U_3 \hat{Z}_2 V_3^H V_{1(4)}^H$ in MLSSM. \mathbf{R}_1 can be found from QR decompositions of the $\hat{Z}_{1(4)}$, $\hat{Z}_3 V_{1(4)}^H$, and $\hat{Z}_2 V_3^H V_{1(4)}^H$ terms, where the second and third terms are a lot smaller than that in the expression for $Z_{1(4)}$ and hence allow savings in the QR decomposition operations.

3 NUMERICAL RESULTS

In this chapter, an observation of the effect of adding the S-EFIE and GC solver formulations on accuracy and condition numbers is first discussed. Next, the new combined formulation accuracy is compared to an industry software evaluation alongside S-EFIE and GC solver. The combined formulation accuracy is also examined across different separation delta. The effect of varying the separation delta on the condition numbers of the combined S-EFIE and GC solver formulation is then considered. Finally, the scalability of MFD in the solution of the geometries discussed in this thesis is considered.

3.1 Effects of Combined S-EFIE and GC Solver Formulation on Conditioning

The results in Table 2 show that the condition numbers of S-EFIE and GC solver could be significantly decreased using the precondition strategy in Effects of Far Interactions. Nonetheless, the condition number for S-EFIE is still very high to be of good use, whilst GC solver has a condition number that is relatively good. A combined formulation was explored to see if the conditioning could be enhanced. Thus, the S-EFIE and GC formulation system matrices were added term-by-term with the charge neutrality constraint for S-EFIE removed. Thus, the resulting combined system matrix is square. The combined system matrix is then preconditioned and scaled.

The resulting system matrix is examined for its conditioning behavior in relation to mesh density compared to S-EFIE and GC solver formulations. The results are shown in Figure 22. The results indicate a conditioning that is superior to S-EFIE or GC solver alone. This suggest the combined S-EFIE and GC solver formulation as a better alternative pairing with MFD which benefits from a low condition number formulation to perform optimally.

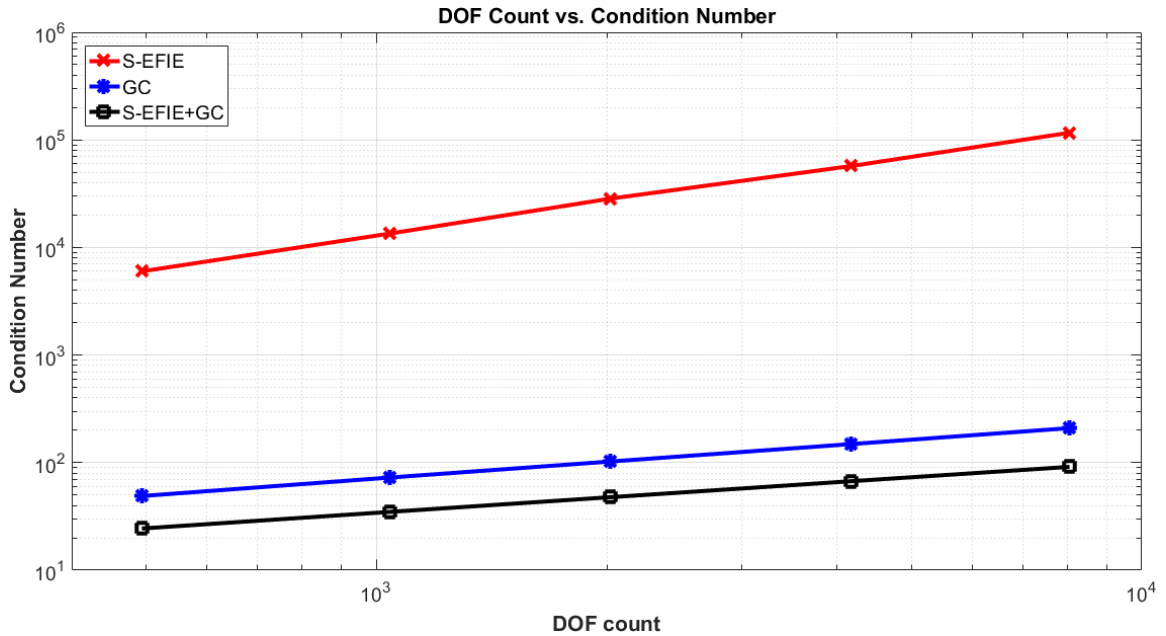


Figure 22: Condition number comparison for S-EFIE, GC solver and combined S-EFIE and GC solver formulations.

3.2 Accuracy across Formulations

The industry software package Q3D Extractor is used as a benchmark to check the accuracy of the capacitance computation using S-EFIE, GC solver and the combined S-EFIE and GC solver formulation, which is henceforth referred to as S-EFIE+GC. The geometry considered is a 10m-by-10m parallel square plate capacitor with 0.002m separation delta. Therefore, the aspect ratio is 5000. Q3D Extractor was set to evaluate the capacitance of this geometry with 19448 DOFs and the resulting capacitance is taken as benchmark to compare against the formulations for accuracy. The resulting capacitance was 443.25nF.

In this investigation, it was found from dense fill experiments that both S-EFIE, GC solver, and S-EFIE+GC formulations yield results that are in very good agreement with that of the Q3D Extractor software package from ANSYS. Note also that S-EFIE, GC solver and S-EFIE+GC are in very good agreement. The differences are tabulated in

Table 3. The observation is also that the error trends lower as the mesh density, i.e. DOF count, increases in all 3 formulations.

Table 3: Result comparison of Q3D Extractor with S-EFIE, GC solver and S-EFIE+GC. Geometry is a 10m-by-10m parallel square plate capacitor with 0.002m separation delta.

DOF Count	Q3D (nF)	Result (nF)			Error (%)		
		S-EFIE	GC	S-EFIE+GC	S-EFIE	GC	S-EFIE+GC
494	443.25	443.02	443.02	443.02	0.05080	0.05080	0.05080
1042	443.25	443.04	443.04	443.04	0.04688	0.04688	0.04688
2022	443.25	443.06	443.06	443.06	0.04239	0.04239	0.04239
4174	443.25	443.08	443.08	443.08	0.03746	0.03746	0.03746
8046	443.25	443.10	443.10	443.10	0.03350	0.03350	0.03350

3.3 S-EFIE+GC Accuracy in Relation to Separation Delta

Q3D Extractor is again used as benchmark and 3 separation deltas were considered; 0.002m, 0.001m and 0.0002m. The parallel square plate size remains at 10m-by-10m. Hence, the aspect ratios are 5000, 10000, and 50000. The DOF count for the geometries are respectively 19448, 23340, and 19416. The capacitance, through Q3D Extractor, were 443.25nF, 885.91nF, and 4427.7nF respectively.

The DOF count vs. percentage error is graphed for S-EFIE+GC for the 3 separation deltas and shown in Figure 23. The Q3D Extractor and S-EFIE+GC are seen to converge as DOF count increases also the results are better as the separation delta decreases.

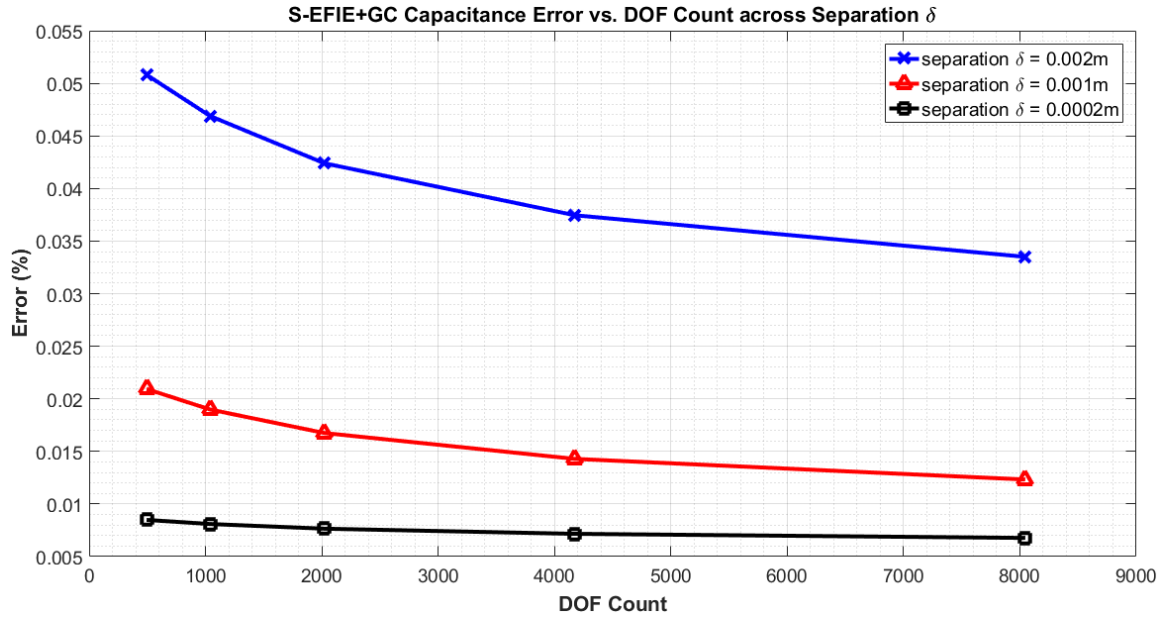


Figure 23: S-EFIE+GC formulation error relative to Q3D across 3 separation deltas for the same parallel square plate capacitor.

3.4 S-EFIE+GC Conditioning in Relation to Separation Delta

The conditioning of S-EFIE+GC as the separation delta decreases is also explored. Figure 24 shows the relation.

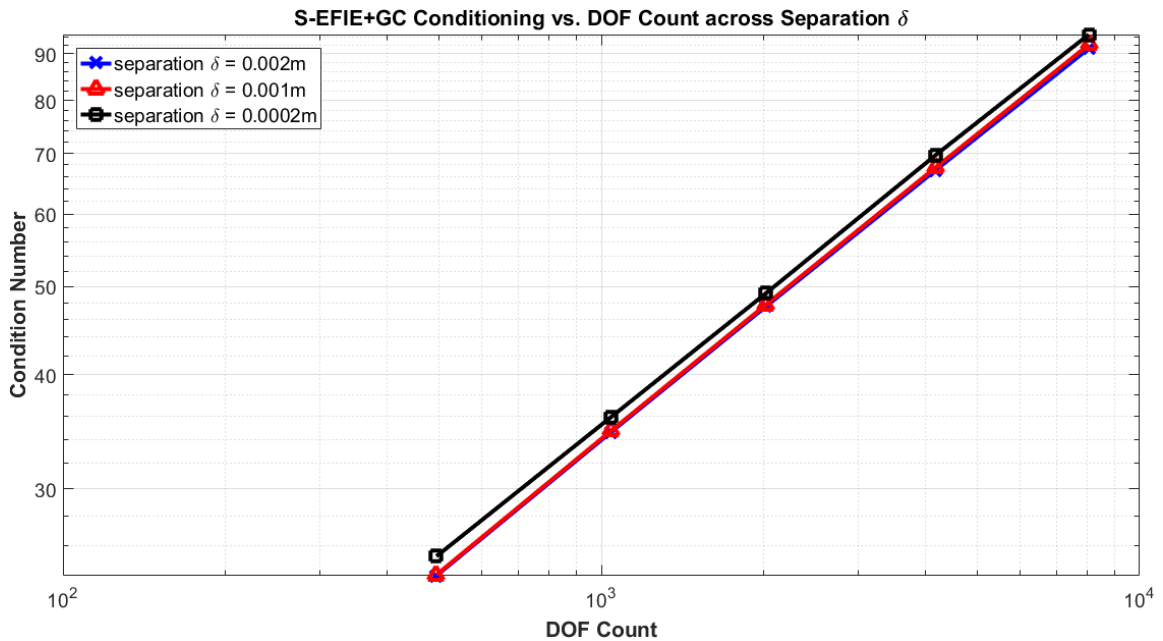


Figure 24: S-EFIE+GC conditioning performance as separation delta decreases.

3.5 S-EFIE+GC Integrated with MFD Accuracy and Scalability Data

The accuracy is first explored. Q3D Extractor values and methodology from S-EFIE+GC Accuracy in Relation to Separation Delta are replicated in this section. The results are shown in Figure 25. The trend from dense fill seems to carry to integration with MFD. It must be remarked that the results published here are the results of MFD integrated with S-EFIE+GC formulation without preconditioning. Therefore, the results may not be at the optimal. The preconditioning that has been proposed thus far is easily implemented on a dense fill execution. However, in integration with MFD, a separate mechanism that allows MFD to discern whether a pair of source and field interactions approximate that explained in “Effects of Far Interactions” remains to be implemented in MFD. This may be possible to integrate in the near fill step of MLSSM in MFD.

Next, the fill operation count versus DOF count between a dense fill run of S-EFIE+GC and a S-EFIE+GC with MFD run is shown in Figure 26. The dense fill operation naturally scales as $O(n^2)$. The S-EFIE+GC with MFD seems to suggest a $O(n)$ scalability. This is followed by the memory usage of MLSSM in Figure 27.

The LOGOS factorization time follows a $O(n^x)$ trend where $x < 2$. This is shown in linear scale in Figure 28. The LOGOS solve time is shown in Figure 29.

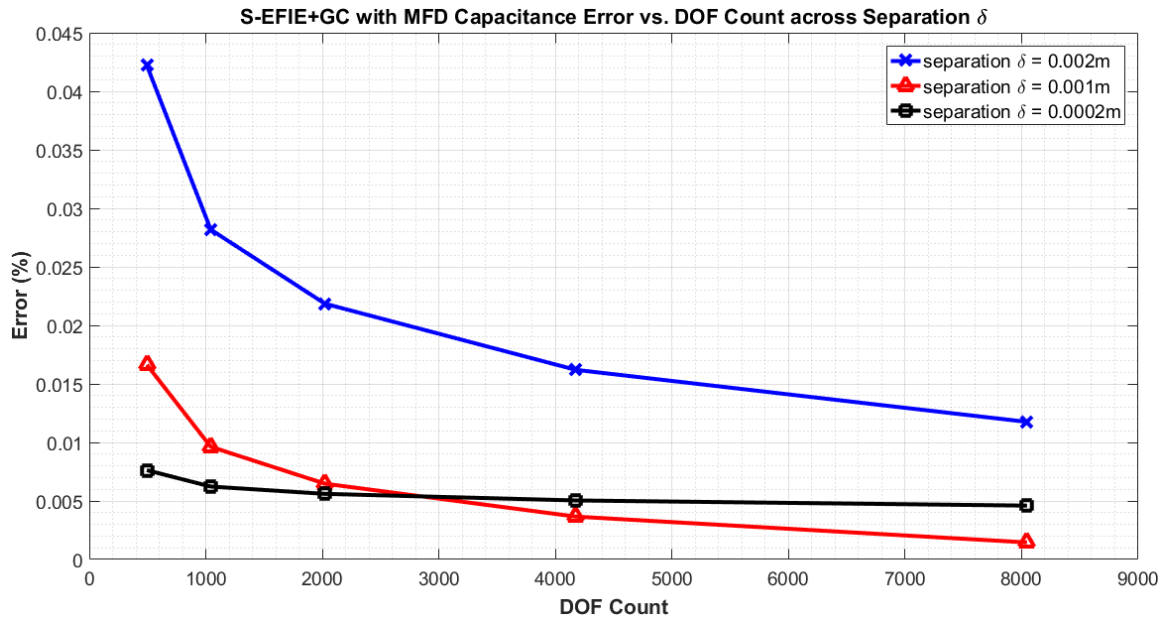


Figure 25:S-EFIE+GC with MFD formulation error relative to Q3D across 3 separation deltas for the same parallel square plate capacitor.

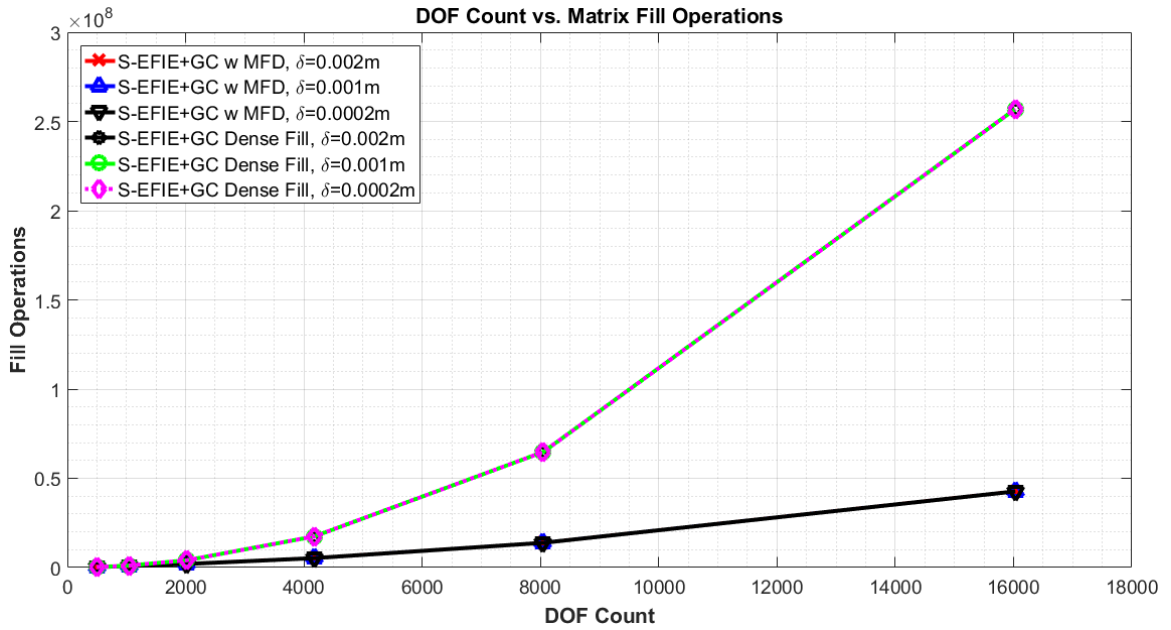


Figure 26:DOF count versus fill operation scalability of S-EFIE+GC integrated with MFD compared to S-EFIE+GC dense fills.

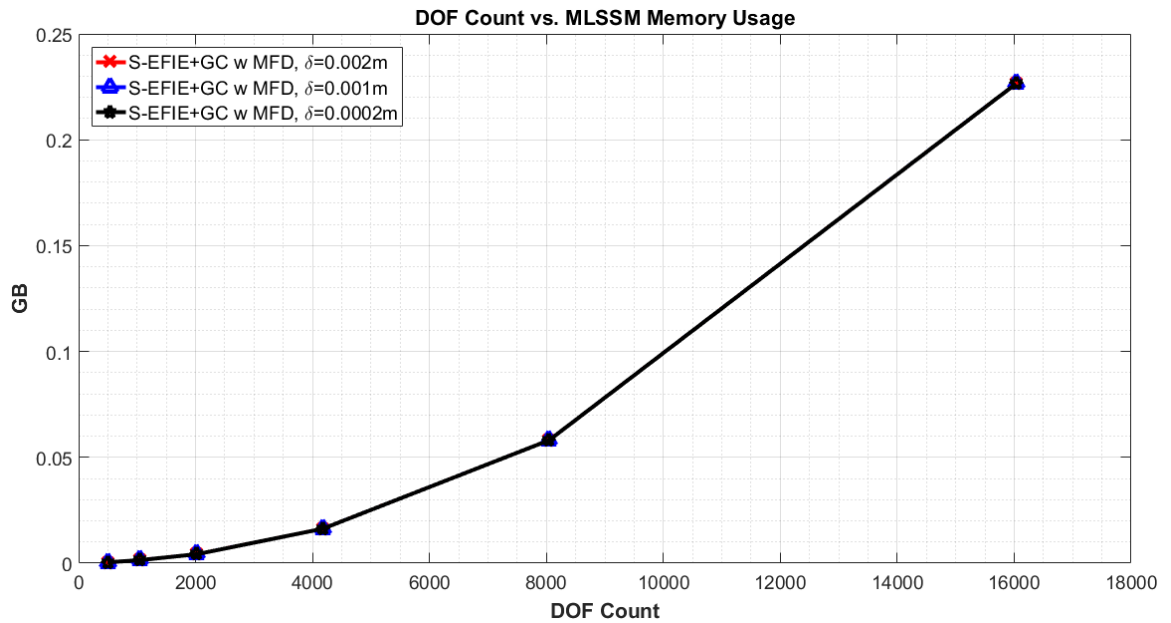


Figure 27:MLSSM memory usage across different separation delta and DOF count.

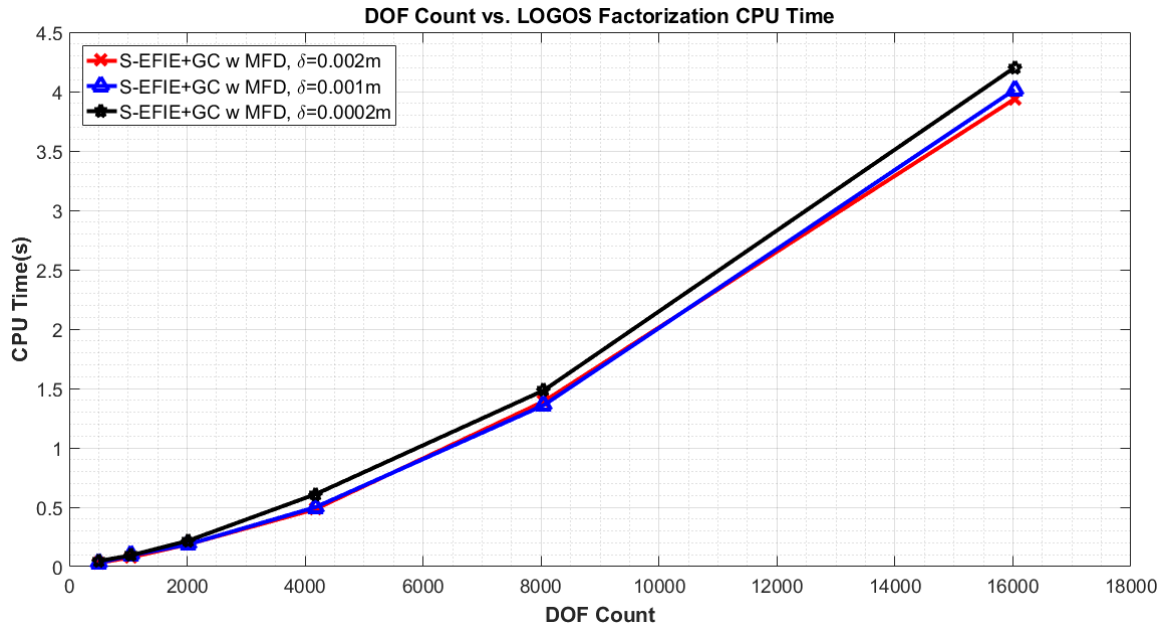


Figure 28:DOF count versus LOGOS factorization CPU time.

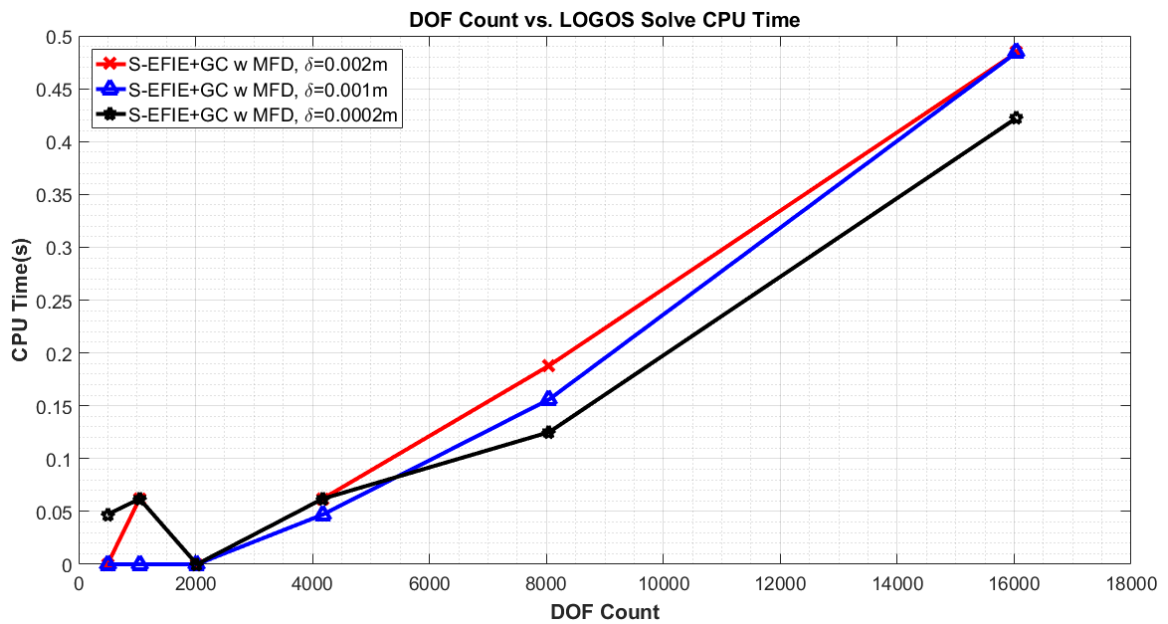


Figure 29:DOF count versus LOGOS solve CPU time.

3.6 AEFIEH-S with MFD Solution Accuracy

As an added consideration, AEFIEH-S is also examined. The bistatic RCS for a PEC sphere of 1-meter radius due to an incident uniform plane wave electric field with incident direction $-\hat{z}$ and polarization in the \hat{x} direction at 2 incident wavelengths 1.5m and 125m computed analytically [23] were used as benchmark. The results of an AEFIEH-S dense fill run

and AEFIEH-S with MFD run were compared to the benchmark and shown in Figure 30 and Figure 31.

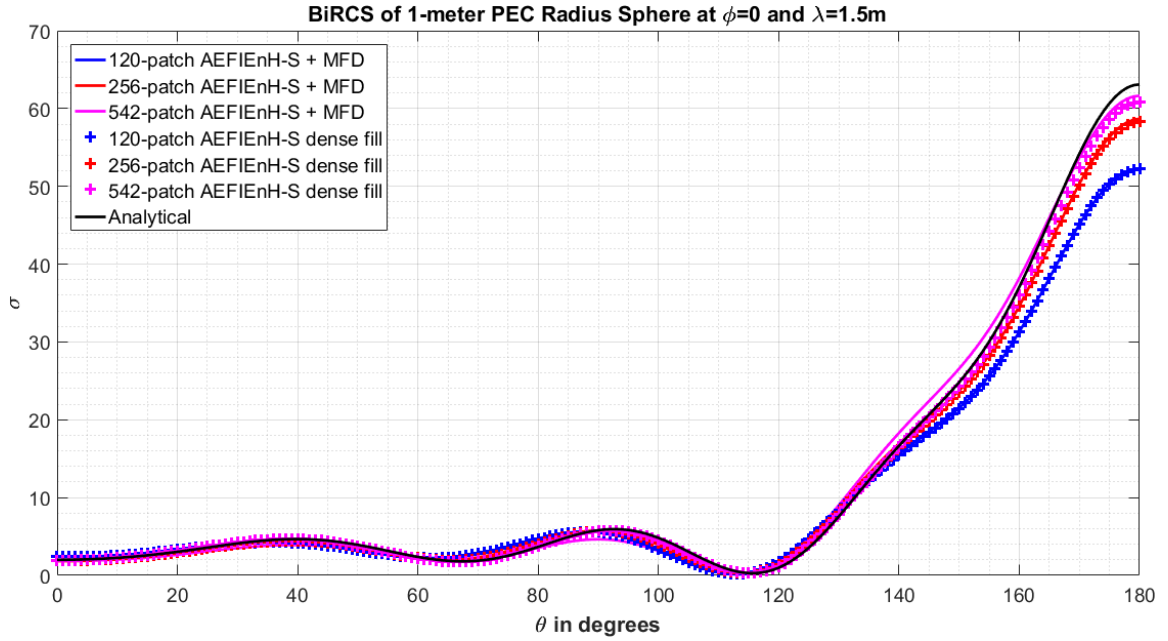


Figure 30: AEFIEH-S dense run and with MFD run against analytical result for 1-m radius PEC sphere at 1.5m wavelength.

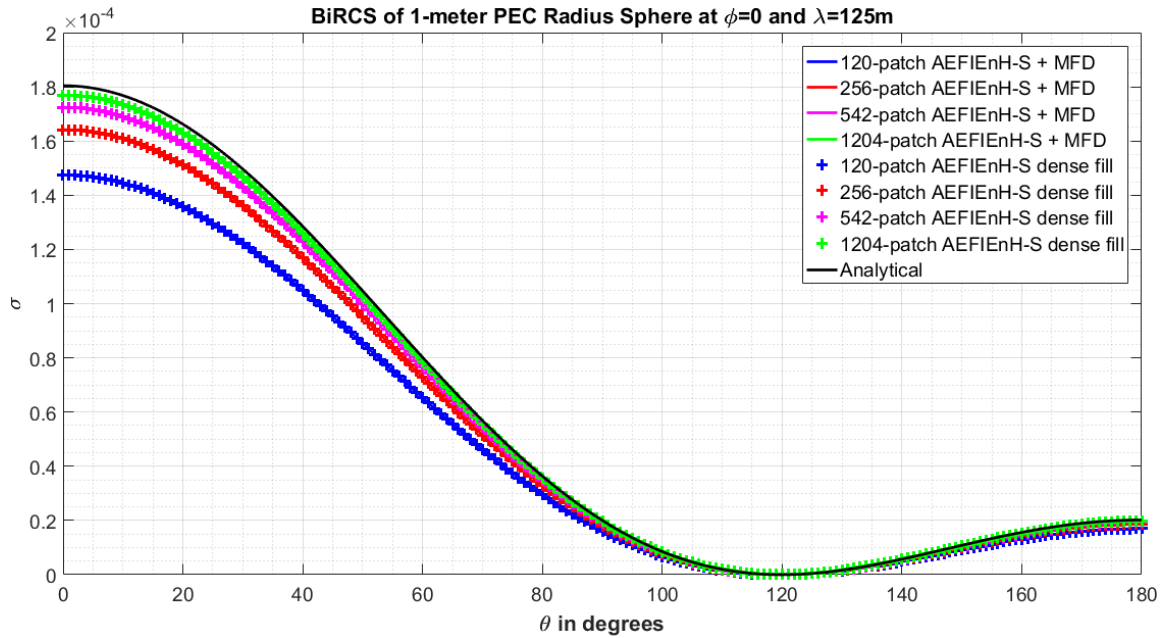


Figure 31: AEFIEH-S dense run and with MFD run against analytical result for 1-m radius PEC sphere at 125m wavelength.

4 CONCLUSION

The genesis for the work underlying this thesis was the problem encountered by the industry when dealing with geometries with high aspect ratios. In the investigation, 2 main problems were found that needed to be resolved to move forward. These were the slow convergence of the adaptive quadrature evaluations on interactions between triangle patches that are very closely located. The high conditioning of the system matrix for the formulations was another obstacle towards integration with MFD which thrives on formulations with low conditioning.

The first problem was resolved by using potential integrals in the static case. The extended Duffy transform whilst slower in comparison to potential integrals allows the potential to apply the formulations to quasi-static cases where the excitation is non-static.

The investigation also led to an understanding of the underlying physics that is causing the poor conditioning of the system matrices for such geometries. That is, as the field point is far removed from the source triangles that pair up and appear to cancel each other in charges, the system matrix will appear to look rank deficient and hence contribute to a singular matrix. The preconditioning strategy has seemed to prove the hypothesis in dense fill scenarios and motivate a preconditioning strategy in MFD as MLSSM fills are being done to alleviate the problem.

Finally, the pairing of MFD with the S-EFIE+GC formulation seem to show significant savings in memory usage as well as fill operations which remains to be the main time-consuming operation. The solve and factorization time of LOGOS seem to scale in $O(n^x)$ where $x < 2$. It must be noted that at the time of the posted results, the preconditioning strategy has not been implemented in MFD. Thus, this suggests that with preconditioning developed into MFD the results may exceed the performance reported to date.

REFERENCES

- [1] Balanis, Constantine A. *Advanced Engineering Electromagnetics*. Wiley, 1989. Print
- [2] Xu, Xin, "MODULAR FAST DIRECT ANALYSIS USING NON-RADIATING LOCAL-GLOBAL SOLUTION MODES" (2008). University of Kentucky Doctoral Dissertations. Paper 690.
- [3] Jin, Jian-Ming. *Theory and Computation of Electromagnetic Fields*. Wiley, 2010. Print
- [4] J. Cheng, R. J. Adams, J. C. Young, M. A. Khayat, "Augmented EFIE With normally constrained magnetic field and static charge extraction", *IEEE Trans. Antennas Propag.*, vol. 63, no. 11, pp. 4952-4963, Nov. 2015.
- [5] Z.-G. Qian, W.C. Chew, "Fast Full-Wave Surface Integral Equation Solver for Multiscale Structure Modeling", *IEEE Trans. Antennas Propag.*, vol. 57, pp. 3594-3601, 2009.
- [6] Z.-G. Qian, W. C. Chew, "Enhanced A-EFIE with perturbation method", *IEEE Trans. Antennas Propag.*, vol. 58, no. 10, pp. 3256-3264, Oct. 2010.
- [7] W. C. Chew, M. S. Tong, and B. Hu, *Integral Equation Methods for Electromagnetic and Elastic Waves*. Morgan and Claypool, 2008
- [8] K. Sarabandi, *EECS 730 Lecture Notes*. University of Michigan, Ann Arbor, 2009
- [9] K. Cools, F. P. Andriulli, F. Olyslager, and E. Michielssen, "Nullspaces of MFIE and calderon preconditioned EFIE operators applied to toroidal surfaces," *IEEE Trans. Antennas Propag.*, vol. 57, no. 10, pp. 3205–3215, Oct. 2009.
- [10] S. M. Rao, D. R. Wilton, and A.W. Glisson, "Electromagnetic scattering by surfaces of arbitrary shape," *IEEE Trans. Antennas Propag.*, vol. AP-30, pp. 409–418, May 1982. F. P.
- [11] Andriulli et al., "A multiplicative Calderon preconditioner for the electric field integral equation," *IEEE Trans. Antennas Propag.*, vol. 56, no. 8, pp. 2398–2412, Aug. 2008.
- [12] S. N. Makarov, *Antenna and EM Modeling with Matlab*. Wiley, 2002
- [13] J.-F. Lee, R. Lee, R. J. Burkholder, "Loop star basis functions and a robust preconditioner for EFIE scattering problems", *IEEE Trans. Antennas Propag.*, vol. 51, no. 8, pp. 1855-1863, Aug. 2003.
- [14] Duffy, M. G., "Quadrature over a pyramid or cube of integrands with a singularity at a vertex", *SIAM J. Numer. Anal.*, 19(6), 1260–1262, 1982.
- [15] D. Wilton, A. Glisson, D. Schaubert, O. Al-Bundak, C. Butler, "Potential integrals for uniform and linear source distributions on polygonal and polyhedral domains", *IEEE Trans. Antennas Propag.*, vol. AP-32, no. 3, pp. 276-281, Mar. 1984.

- [16] Young, John C. "RE: 5-hop check" Message to Chee Kean Chang. 10 January 2017. E-mail.
- [17] Deng, Shaozhong, *Math 5172 Lecture Notes*. University of North Carolina, Charlotte, 2010.
- [18] X. Xu, R. J. Adams, "Sparse matrix factorization using overlapped localizing LOGOS modes on a shifted grid", *IEEE Transactions on Antennas and Propagation*, vol. 60, no. 3, 2012.
- [19] R. J. Adams, Y. Xu, X. Xu, J. s. Choi, S. D. Gedney and F. X. Canning, "Modular Fast Direct Electromagnetic Analysis Using Local-Global Solution Modes," in *IEEE Transactions on Antennas and Propagation*, vol. 56, no. 8, pp. 2427-2441, Aug. 2008.
- [20] F. X. Canning and K. Rogovin, "Simply Sparse, a general compression/solution method for MoM programs," *IEEE Antennas and Propagation Society International Symposium (IEEE Cat. No.02CH37313)*, 2002, pp. 234-237 vol.2.
- [21] Y. Xu, X. Xu and R. J. Adams, "A Sparse Factorization for Fast Computation of Localizing Modes," in *IEEE Transactions on Antennas and Propagation*, vol. 58, no. 9, pp. 3044-3049, Sept. 2010.
- [22] S. Kurz, O. Rain, and S. Rjasanow, "The Adaptive Cross-Approximation Technique for the 3-D Boundary-Element Method," in *IEEE Trans. Magn.*, 38(2): 421-424, 2002.
- [23] Roger F. Harrington, "Spherical Wave Functions," in *Time-Harmonic Electromagnetic Fields*, 1, Wiley-IEEE Press, 2001, pp.264-316

VITA

Chee Kean Chang

Education

- B. Sc. in Electrical Engineering, University of Kentucky, Lexington, 2001-2004

Work Experience

- Systems Analyst, Ashland, Inc., Lexington, KY, 2004-2010
- Product Design Engineer, Intel, Malaysia, 2011-2012
- Systems Design Engineer, AMD, Austin, TX, 2012-2016